The Astrophysical Journal, 820:62 (18pp), 2016 March 20 doi:10.3847/0004-637X/820/1/62

NONRELATIVISTIC PERPENDICULAR SHOCKS MODELING YOUNG SUPERNOVA REMNANTS: NONSTATIONARY DYNAMICS AND PARTICLE ACCELERATION AT FORWARD AND REVERSE SHOCKS

Volkmar Wieland[1], Martin Pohl[1,2,5], Jacek Niemiec[3], Iman Rafighi[1], and Ken-Ichi Nishikawa[4]
[1] Institute of Physics and Astronomy, University of Potsdam, D-14476 Potsdam, Germany; marpohl@uni-potsdam.de
[2] DESY, D-15738 Zeuthen, Germany
[3] Instytut Fizyki Jądrowej PAN, ul. Radzikowskiego 152, 31-342 Kraków, Poland
[4] Department of Physics, University of Alabama in Huntsville, Huntsville, AL 35899, USA
Received 2015 May 6; accepted 2016 February 15; published 2016 March 17

ABSTRACT

For parameters that are applicable to the conditions at young supernova remnants, we present results of two-dimensional, three-vector (2D3V) particle-in-cell simulations of a non-relativistic plasma shock with a large-scale perpendicular magnetic field inclined at a 45° angle to the simulation plane to approximate three-dimensional (3D) physics. We developed an improved clean setup that uses the collision of two plasma slabs with different densities and velocities, leading to the development of two distinctive shocks and a contact discontinuity. The shock formation is mediated by Weibel-type filamentation instabilities that generate magnetic turbulence. Cyclic reformation is observed in both shocks with similar period, for which we note global variations due to shock rippling and local variations arising from turbulent current filaments. The shock rippling occurs on spatial and temporal scales produced by the gyro-motions of shock-reflected ions. The drift motion of electrons and ions is not a gradient drift, but is commensurate with $\boldsymbol{E} \times \boldsymbol{B}$ drift. We observe a stable supra-thermal tail in the ion spectra, but no electron acceleration because the amplitude of the Buneman modes in the shock foot is insufficient for trapping relativistic electrons. We see no evidence of turbulent reconnection. A comparison with other two-dimensional (2D) simulation results suggests that the plasma beta and the ion-to-electron mass ratio are not decisive for efficient electron acceleration, but the pre-acceleration efficacy might be reduced with respect to the 2D results once 3D effects are fully accounted for. Other microphysical factors may also play a part in limiting the amplitude of the Buneman waves or preventing the return of electrons to the foot region.

Key words: acceleration of particles – instabilities – ISM: supernova remnants – methods: numerical – plasmas – shock waves

1. INTRODUCTION

Collisionless shocks in space are sites of efficient particle acceleration. While direct in situ studies of these shocks are possible only in interplanetary space, understanding the properties of high-Mach-number shocks in supernova remnants (SNRs) is highly desirable because SNRs are suspected to supply a significant fraction of cosmic rays. The emission of freshly accelerated particles has been observed for many years (Reynolds 2008). The acceleration process that is likely dominant is diffusive shock acceleration (DSA), or first-order Fermi acceleration (Fermi 1949). Charged particles scatter off magnetic inhomogeneities, e.g., in the form of magneto-hydrodynamic (MHD) waves, in the upstream and downstream regions of the shock, which isotropizes their distribution function in each region. If particles have enough energy to cross the shock front, i.e., if their mean free path is large enough to "see" the shock as a sharp discontinuity, then they systematically gain energy with each cycle of shock crossing, and the relation between the probabilities of escape and of return to the shock determines what spectrum the particles assume (Blandford & Eichler 1987).

Of relevance to the process is the structure of the shocks, the electromagnetic field amplitudes at the shocks, and the local pre-acceleration processes that separate particles from the quasithermal bulk. The shock structure is typically driven by ions, and therefore has ion length scales. Electrons have small plasma and gyration scales compared to ions, and so electron pre-acceleration is a particularly interesting problem.

Here, we study perpendicular shocks whose structure is driven by ion reflection, leading to a steep density ramp and various instabilities operating in the foot region ahead of the ramp (Bale et al. 2005; Treumann & Jaroschek 2008a; Treumann 2009). Depending on the Alfvénic Mach number, M_A, quasi-standing whistler waves may be found in the foot region (Hellinger et al. 2007) and accelerate electrons (Riquelme & Spitkovsky 2011). The large-scale motion of ions can lead to shock surfing acceleration (SSA; Sagdeev & Shapiro 1973) or shock-drift acceleration (SDA; Krauss-Varban & Wu 1989). In their original design, these two process would not significantly affect electrons (Treumann & Jaroschek 2008b); however, see Guo et al. (2014). Instead, appropriate instabilities, solitary structures, or similar structures are required, an example of which is the Buneman instability between reflected ions and incoming electrons. The result would be strong electron heating and acceleration in the foot region (Shimada & Hoshino 2000), possibly followed by secondary accelerations through adiabatic processes or ion-acoustic instability (Kato & Takabe 2010; Matsumoto et al. 2012, 2013).

Studying electron acceleration requires that electron scales be resolved, and so we conduct particle-in-cell (PIC) simulations in two-dimensional, three-vector (2D3V) configuration, i.e., allowing gradients in two dimensions but following all three vector components. Hybrid simulations (e.g., Caprioli & Spitkovsky 2014) allow us to study the behavior on longer

[5] Author to whom any correspondence should be addressed.

timescales and large spatial scales, but provide no information on electron dynamics. Having investigated unmagnetized shocks and weakly magnetized strictly parallel shocks before (Niemiec et al. 2012, hereafter N2012), here we report on simulations of strictly perpendicular ($\theta_{Bn} = 90°$) shocks, leaving the results for oblique shocks to a future publication.

We concentrate on the parameter regime typical of young SNRs, as opposed to, e.g., heliospheric conditions and low-Mach-number non-relativistic shocks (e.g., Umeda et al. 2008; Riquelme & Spitkovsky 2011; Guo et al. 2014). We consider large sonic (cold plasmas with $\beta_e \ll 1$) and Alfvénic Mach numbers, M_s and M_A, and sub-relativistic plasma collision velocities allowing for Weibel-type (filamentation) instabilities to occur (Kato & Takabe 2008, 2010; Niemiec et al. 2012). Our simulations thus complement the two-dimensional (2D) PIC simulations of Matsumoto et al. (2013) and Matsumoto et al. (2015), who have covered the parameter range $\beta_e \simeq 0.5$ and both sonic and Alfvénic Mach numbers around 40. In contrast to all earlier studies of high-Mach-number perpendicular shocks using either in-plane or out-of-plane configurations of the homogeneous magnetic field, and often finding a different efficiency of, e.g., electron heating by electrostatic modes (Amano & Hoshino 2009b), we set our regular magnetic field component at an angle of 45° to the simulation plane. We expect that such a setup will better approximate the physics of fully three-dimensional (3D) systems. We follow the shock evolution for 20 ion cyclotron times, $t\Omega_i = 20$, which is considerably longer than other published PIC studies. We have also introduced a setup that minimizes artificial electromagnetic transients during shock launching, which may influence the upstream medium.

In numerical simulations, collisionless shocks can be initiated in a number of ways. The most widely used techniques are the injection method (Burgess et al. 1989), the flow–flow method (Omidi & Winske 1992), the relaxation method (Leroy et al. 1981, 1982), and the magnetic-piston method (Lembege & Savoini 1992). The injection method uses a plasma beam that is reflected off a conducting wall. The reflected particle beam interacts with the incoming plasma and a shock is created. Implicitly, this method assumes an infinitely sharp contact discontinuity (CD), whereas in a collisionless plasma the CD has a finite width and internal structure. In the flow–flow method, two counterstreaming plasma beams are continuously injected at the sides of the computational box and couple to form in time a system of two shocks separated by a CD. This setup offers more freedom in the choice of the physical parameters for the colliding plasmas. This method is also physically more accurate than the injection method as it avoids the assumption of an infinitely sharp CD. The relaxation method uses a simulation box filled with plasma that is separated by a discontinuity into two uniform plasma slabs that are supposed to initially satisfy the shock jump conditions (see also Umeda & Yamazaki 2006). Finally, the magnetic-piston method applies an external current pulse that induces an electromagnetic field transient which propagates in the plasma to develop into a shock (for a more detailed account of the shock excitation methods see, e.g., Lembege 2003, p. 54).

In our simulations, we use a flow–flow method of shock excitation which allows us to investigate the dynamics of both forward and reverse shock at the same time. The asymmetric slab-collision setup used in Niemiec et al. (2012) is further developed in the present study to include a new setup for perpendicular shocks that avoids having sharp gradients in the motional electric fields with opposite sign at the CD. Such gradients work as an artificial dipole antenna, and thereby emit a strong electromagnetic pulse whose presence in the system may limit the veracity of the simulation in the initial, as well as the nonlinear, stage of system evolution.

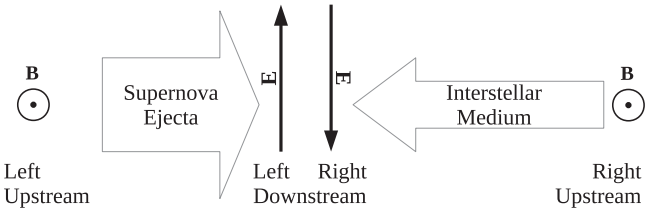

Figure 1. Illustration of the setup for a perpendicular shock showing the directions of motion of the two plasma slabs and the motional electric fields for a magnetic field oriented out of the plane of the figure.

We describe updates to our simulation model and the setup in Section 2. The results of the simulation are presented in Section 3. A summary and discussion conclude the paper in Section 4.

2. SIMULATION SETUP

2.1. New Setup for Perpendicular Shocks

The numerical grid is initially filled with two plasma slabs of uniform density that are separated by a void and move toward each other. Once they collide, a system of two shocks and the CD is formed. Note that in contrast to the injection and relaxation methods, the CD is self-consistently developed and not initially assumed.

To set up a magnetized plasma system, one may establish a homogeneous magnetic field $\boldsymbol{B}_0$ in the entire simulation box perpendicular to the streaming direction of the plasma beams. The magnetic field is meant to be frozen into the moving plasma, i.e., in the rest frame of the plasma $\boldsymbol{E}' = 0$ and $\boldsymbol{B}'$ are the electric and magnetic field. In the simulation frame, nonrelativistic Lorentz transformations yield $\boldsymbol{E} = -\boldsymbol{v} \times \boldsymbol{B}'$ and $\boldsymbol{B} = \boldsymbol{B}'$, where $\boldsymbol{v}$ is the streaming velocity of the plasma slabs. In our simulation, the two plasmas have streaming velocities $\boldsymbol{v}_L = v_{L,x}\,\hat{\boldsymbol{x}}$ and $\boldsymbol{v}_R = v_{R,x}\,\hat{\boldsymbol{x}}$, where the indices L and R refer to the initial position of the plasmas on the *left* and *right* sides of the simulation box, respectively, and the magnetic field is aligned in the y–z-direction, which leads to

$$\begin{pmatrix} E_{L,x} \\ E_{L,y} \\ E_{L,z} \end{pmatrix} = \begin{pmatrix} 0 \\ v_{L,x}\,B_{L,z} \\ -v_{L,x}\,B_{L,y} \end{pmatrix} \quad (1)$$

and

$$\begin{pmatrix} E_{R,x} \\ E_{R,y} \\ E_{R,z} \end{pmatrix} = \begin{pmatrix} 0 \\ v_{R,x}\,B_{R,z} \\ -v_{R,x}\,B_{R,y} \end{pmatrix}. \quad (2)$$

In the simulations described here, $\boldsymbol{B}_L = \boldsymbol{B}_R$. Since $v_{L,x}$ and $v_{R,x}$ have opposing signs, the motional electric field has opposing signs in the two plasmas, which is illustrated in Figure 1. Without further modification, this setup would lead to a large value of $\nabla \times \boldsymbol{E}$ at the edges of the plasma slabs in the middle of the simulation box, which through the corresponding $\partial \boldsymbol{B}/\partial t$

Table 1
Basic Parameters of the Double-shock Simulation and Derived Shock Properties

	Left Dense Plasma Reverse Shock	Right Dilute Plasma Forward Shock
Skin length	$\lambda_{se,L}$ 7.9Δ	$\lambda_{se,R}$ 25Δ
Thermal speed $v_{e,th}$	$0.002\ c$	$0.002\ c$
Streaming speed	$v_{L,x}$ $0.0354\ c$	$v_{R,x}$ $-0.354\ c$
Alfvén speed	$v_{A,L}$ $0.00447\ c$	$v_{A,L}$ $0.0142\ c$
Shock speed in upstream frame	$v_{sh,L}$ $-0.127\ c$	$v_{sh,R}$ $0.39\ c$
Mach numbers M_A M_s	 28.5 252	 27.6 755

would induce an electromagnetic transient that may limit the veracity of the simulation.

We developed a setup that avoids this artificial antenna effect by implementing a transition zone between the two slabs. A spatial gradient is imposed in the perpendicular magnetic field components B_y and B_z in the front layers of the colliding plasma slabs that tapers the field off until it vanishes at the interface to the plasma-free area, which can initially separate the slabs. A corresponding tapering of the motional electric field naturally results. The non-zero $\nabla \times \boldsymbol{B}$ is compensated for by a current sheet in which ions drift relative to the electrons. A detailed mathematical description and illustration of this new setup can be found in the Appendix.

Figure 21 in the Appendix compares the stability in the particle and field density of the new setup with the conventional scenario of a jumping motional electric field, E_y, due to a constant perpendicular magnetic field, B_z. The new setup is very stable over many time steps, whereas for the standard setup with constant magnetic field one can clearly see a transient in the electric field, which is emitted in the middle of the simulation box and eventually perturbs the magnetic field.

2.2. Simulation Parameters

For ease of comparison, we basically used the same numerical parameters as in simulation run M1 in N2012. The parameters are chosen such that our simulation results may be applied to plasma shocks formed at young SNRs. The two plasma slabs are composed of equal numbers of electrons and ions, which are initialized at the same location in order to make the system initially neutral. The two slabs have different densities with a density ratio 10, and hence their plasma frequencies differ by a factor of $\sqrt{10} \simeq 3.1$. We use 10 particles per cell per particle species for both plasma slabs and assign statistical weights to the tenuous-plasma particles to establish the intended density ratio. In order to resolve the characteristic length scales of both the electrons and ions in our simulations, we choose a reduced ion-to-electron mass ratio of $m_i/m_e = 50$.

The main simulation parameters are summarized in Table 1. In our simulation frame, which is the center-of-momentum frame, the *dense* plasma moves to the right, while the *tenuous* plasma moves to the left. The two plasmas collide at a relative speed of $v_{rel} = 0.38\ c$ and in time form a double-shock structure with a CD separating the downstream regions of the two shocks. On account of the similarity with dense ejecta moving into the dilute ambient medium in an SNR, we designate the right shock in the low-density plasma as the forward shock and the left shock as the reverse shock. In time, the CD starts moving in the simulation frame with $v_{CD} = -0.06\ c$ because the system is in momentum balance but not in ram-pressure balance.

Our simulations are performed using a 2D3V model, i.e., we restrict all of the particles to two spatial dimensions while keeping all three components of their velocities. Since the large-scale magnetic field bends the particle trajectories out of the simulation plane, particles have three degrees of freedom and the non-relativistic adiabatic index is $\Gamma = 5/3$. The electrons and ions of both plasmas are initially in thermal equilibrium and cold, thus permitting large sonic Mach numbers, as expected for SNRs. The initially homogeneous magnetic field is aligned perpendicular to the plasma flow and lies in the y–z plane making an angle $\phi = 45°$ with the y-axis, i.e., $\boldsymbol{B} = B_0(0, 1, 1)/\sqrt{2}$. The strength of the magnetic field can also be expressed by the electron cyclotron frequency, $\Omega_e = eB_0/m_e$, whose ratio to the electron plasma frequency of the dense plasma, $\omega_{pe,L} = \sqrt{n_{e,L}e^2/\epsilon_0 m_e}$, is $\Omega_e/\omega_{pe,L} = 0.032$. Here, $n_{e,L}$ is the electron density of the dense plasma, e is the electric charge, and ϵ_0 is the permittivity of the vacuum.

The sonic and Alfvénic Mach numbers given in Table 1 are calculated as the ratios of the shock velocities in the upstream reference frames to the sound and Alfvén speeds in these frames. The sonic Mach numbers are typical for SNRs expanding into a medium with a temperature around a few thousand kelvin. The Alfvénic Mach numbers of our two shocks are considerably lower than the minimum Mach numbers of $M_A \approx 180$ estimated for the real mass ratio $m_i = 1836 m_e$ for shocks in young SNRs to efficiently pre-accelerate electrons (see Equation (8) in Matsumoto et al. 2012). However, for the reduced mass ratio employed in our simulations, we can sample the same physics already at $M_A \geqslant 16$. The Alfvénic Mach numbers in our simulations can thus well represent the conditions at young SNR shocks expanding into a weakly magnetized medium.

The spatial dimensions in our simulation and all figures are given in terms of the electron skin length of the dense plasma $\lambda_{se} \equiv \lambda_{se,L} = c/\omega_{pe,L} = 7.9\Delta$, where Δ is the size of the grid cells. The temporal dimensions are given in terms of the inverse of the upstream ion Larmor frequency $\Omega_i^{-1} = 1582.3\ \omega_{pe,L}^{-1}$. The simulation time is $T = 20\ \Omega_i^{-1} = 31645.5\ \omega_{pe,L}^{-1} = 4472.3\ \omega_{pi,L}^{-1} = 1000\ \Omega_e^{-1}$, which is longer by factors of 4 and 2, respectively, than the simulations described in Kato & Takabe (2010) and Guo et al. (2014).

The transverse size of the simulation box is $L_y = 324.1\ \lambda_{se} = 42.9\ \lambda_{si,L}$ with periodic boundary conditions. Radiative boundary conditions are imposed in the x-direction. We use a so-called moving injector method, in which particles are continuously injected into a small injection layer at the outer edges of the two plasma slabs. The injection layer retreats

from the collision zone as far as necessary to keep all of the streaming or reflected particles and fields within the collision region, but it stays as close as possible such that newly injected particles do not have to travel a long distance without any interaction. The simulation box is thus permitted to grow in the x-direction, reaching a final size of $L_x = 9493.7\ \lambda_{se}$ at the end of the simulation.

The simulation was performed with a modified version of the TRISTAN code (Buneman 1993, pp. 67–84), which was adapted to work in 2D3V and parallelized using MPI (Niemiec et al. 2008). Other modifications include a fourth-order finite-difference time-domain (FDTD) field-pusher with a weak Friedman filter (Friedman et al. 1990; Greenwood et al. 2004), which efficiently filters numerical Cerenkov radiation, and the pusher proposed in Vay (2008), which achieves better energy conservation and less numerical self-heating.

3. SIMULATION RESULTS

3.1. Early-stage Evolution

We remind the reader that the right shock in the dilute plasma is also referred to as the forward shock and the left shock in the dense medium is the reverse shock. Also recall that as our length scale we use the electron skin length, λ_{se}, of the far-upstream dense plasma in the left part of the simulation box. Downstream of the reverse shock, the true skin length is only $\lambda_{se}/2$, and less than that at the density overshoot. In the tenuous plasma on the right, the true skin length is always 3.1 times that in the dense plasma due to the factor of 10 density ratio.

In this section, we present the structure of the two evolving shocks after $T\ \Omega_i = 4.8$, which is comparable to the total time covered in the simulations of Umeda et al. (2008), Kato & Takabe (2010), and Matsumoto et al. (2012). A global picture is offered in Figure 2 where we show profiles of the transversely averaged particle densities and field energy densities, p_x versus x phase-space information, and 2D distributions of the particle density and the magnetic field component B_z.

The CD, now clearly visible at $x \approx 5300\ \lambda_{se}$, moves with a predicted speed of $v_{CD,x} = -0.06\ c$. The forward shock is visible at about $x \approx 5900\ \lambda_{se}$ and the reverse shock is found near $x \approx 5000\ \lambda_{se}$. It is obvious that the two shocks have not propagated very far from the CD, and so the system may not yet be in statistical equilibrium. Nevertheless, the salient features of collisionless shocks are already visible. Noting that the 2D distribution of ions very closely follows that of the electrons, we only show the electron density in the blow-up of the display for the forward shock (Figure 3) and the reverse shock (Figure 4).

In Figure 3, we note the presence of shock-reflected ions, which in a super-critical perpendicular shock may lead to the growth of Buneman modes in the foot of the shock, which can subsequently heat and accelerate the incoming electrons. A Fourier analysis of E_x indeed reveals Buneman waves at $k_\perp\ \lambda_{se} \simeq 0$ and $k_\parallel\ \lambda_{s,e} \simeq 0.8$. Figure 3 indicates that the drift velocity between reflected ions and incoming electrons near $x = 6150\ \lambda_{se}$ is $v_{rel} \simeq 0.4\ c$. We expect the growth of Buneman modes at

$$k_\parallel \simeq \frac{c}{v_{rel}}\ \frac{1}{\lambda_{se,local}} \simeq 2.5\ \frac{1}{3.1\ \lambda_{se}} \simeq 0.8\ \frac{1}{\lambda_{se}}, \qquad (3)$$

which is exactly what is observed. In Equation (3), we have used the local electron skin length, $\lambda_{se,local} = \lambda_{se,R}$, which is $\sqrt{10}$ times that of the dense plasma, λ_{se}.

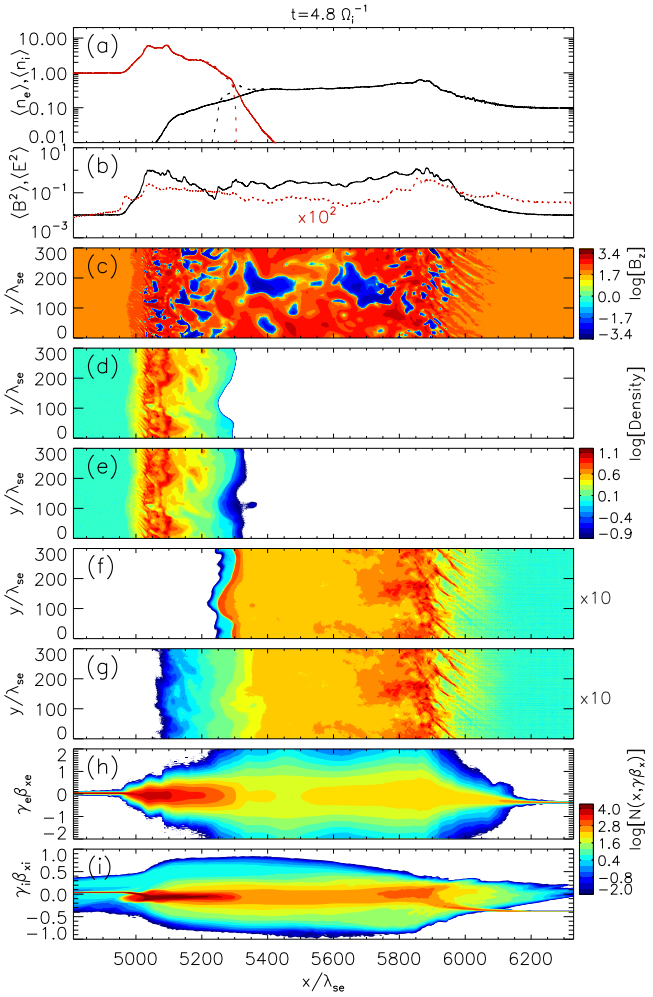

Figure 2. Structure of the plasma collision region at time $t = 4.8\ \Omega_i^{-1}$. Displayed are the profiles of (a) the average particle-number density normalized to the far-upstream density of the dense plasma (red lines: dense plasma, black lines: tenuous plasma; solid lines: ions, dashed lines: electrons), (b) profiles of the average magnetic (solid line) and electric (red dotted line, times factor 100) energy density in simulation units, (c) the amplitude of the magnetic field B_z (in sign-preserving logarithmic scale as $\mathrm{sgn}(B_z)(2 + \log[\max(10^{-2}, |B_z|)])$), the density of dense-plasma electrons (d), dense-plasma ions (e), tenuous-plasma electrons (f), and tenuous-plasma ions (g), all normalized to their far-upstream values, and the longitudinal phase-space distribution of electrons (h) and ions (i).

We follow Matsumoto et al. (2012) in the analysis of this first stage of electron heating. The relative velocity of the incoming electrons and reflected ions must be larger than the thermal speed of the electrons, which leads to the condition

$$M_s \geqslant \frac{1+\alpha}{2}\ \sqrt{\frac{m_i}{m_e}}\ \sqrt{\frac{T_e}{T_i}}, \qquad (4)$$

where α denotes the density ratio of the reflected and incoming ions. Whereas the temperature ratio can deviate from unity on account of physics, the dependence on the mass ratio is important for proper interpretation of simulations that may use a small mass ratio for computational reasons. Matsumoto et al. (2012) write this condition in terms of the Alfvénic Mach number and the electron plasma beta, which we consider to not be helpful because the Alfvén speed cancels in their expression. The magnetic field may be relevant, however, for the energy

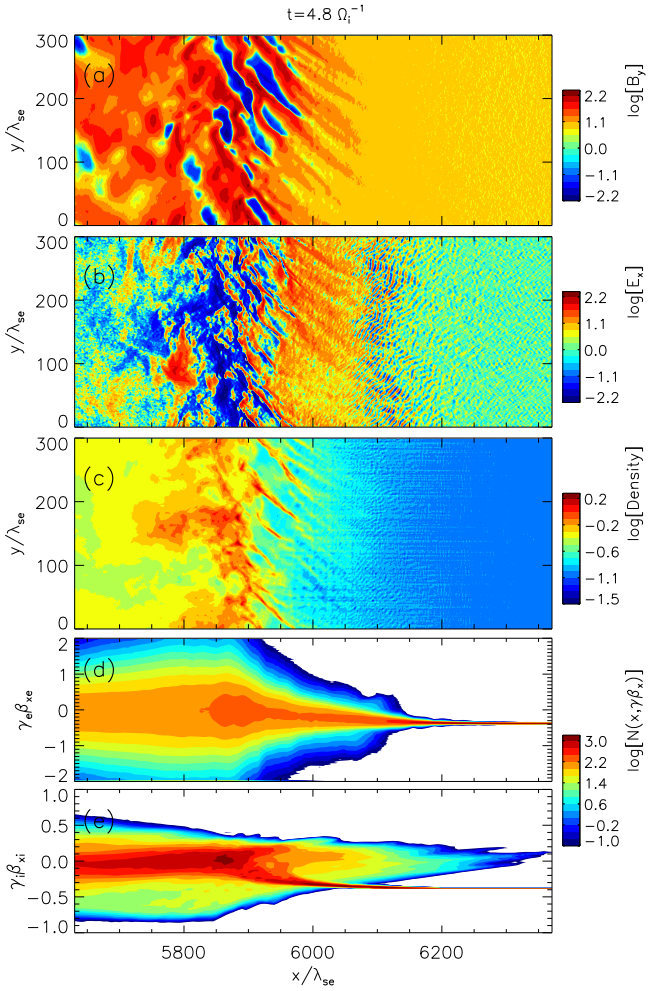

Figure 3. Structure of the forward shock at time $t = 4.8\,\Omega_{\rm i}^{-1}$. Displayed are the distributions of the magnetic field component B_y (a), the electric field component E_x (b), the density of electrons (c), and the longitudinal phase-space distribution of electrons (d) and ions (e).

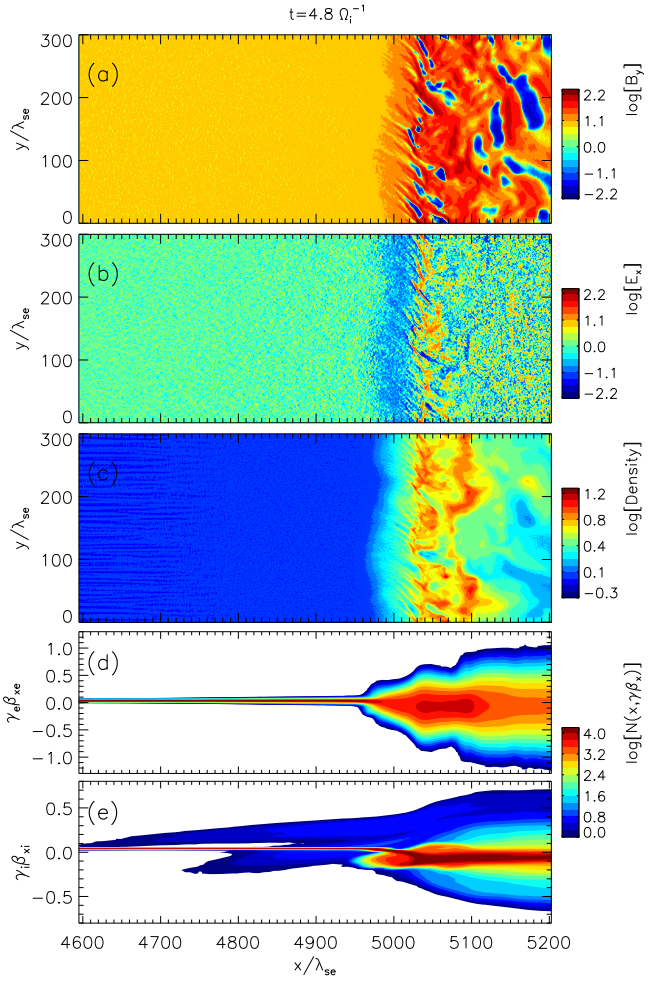

Figure 4. Structure of the reverse shock at time $t = 4.8\,\Omega_{\rm i}^{-1}$. Displayed are the distributions of the magnetic field component B_y (a), the electric field component E_x (b), the density of electrons (c), and the longitudinal phase-space distribution of electrons (d) and ions (e).

gain that electrons may achieve. If we express the momentum increment as the product of the force provided by the Buneman electric field, $E_{\rm B}$, and the Larmor time, $\Omega_{\rm e}^{-1}$, then we find

$$\delta p \simeq m_{\rm e}\, c\, \frac{E_{\rm B}}{B_0}. \tag{5}$$

Assuming isotropization and relating the saturation-level energy density of the electric field to the fraction $0.25(m_{\rm e}/m_{\rm i})^{1/3}$ (Ishihara et al. 1980), we arrive at

$$\delta p_{x,y,z} \simeq \frac{1}{\sqrt{3}}\,\frac{m_{\rm e}\, c\, M_{\rm A}}{1+\alpha}\left(\frac{m_{\rm e}}{m_{\rm i}}\right)^{\frac{2}{3}} \simeq 0.9\, m_{\rm e}\, c, \tag{6}$$

where the last numerical expression is calculated using the parameters of our simulation. This is evidently much more than the spread of the longitudinal phase-space distribution of electrons displayed in Figure 5, in which the peak intensity of the Buneman waves is seen near $x = 6100\,\lambda_{\rm se}$, where the spread in the p_x component increases to only $\sim 0.1\, m_{\rm e}\, c$. The distribution of electrons is reasonably close to Gaussian. The initial acceleration is in the x-direction, and the perpendicular magnetic field provides efficient deflection in the y- or z-direction over a distance of $\sim 20\,\lambda_{\rm se}$. The ion momentum spread in the upstream regions is dominated by the beam of reflected ions.

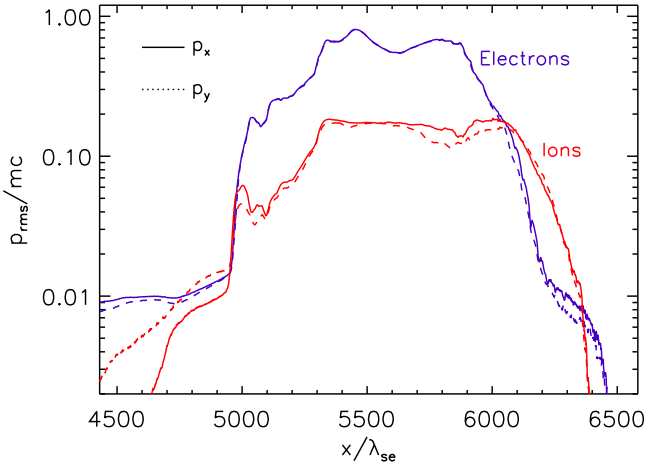

Figure 5. The rms values of the momentum components p_x (solid lines) and p_y (dotted lines) of electrons and ions.

The estimate of Equation (6) may be too optimistic because the electrons lose resonance with the Buneman modes in less than the Larmor time, Ω_e^{-1}. We also note that the total convertable electron drift energy density (Ishihara et al. 1980; Matsumoto et al. 2012), when turned into electron heat, gives only

$$\delta p_{x,y,z} \simeq \frac{1}{\sqrt{3}} \frac{1}{1+\alpha} \frac{v_{\rm sh}}{c} \left(\frac{m_e}{m_i}\right)^{\frac{1}{6}} \simeq 0.1\, m_e\, c, \qquad (7)$$

which is close to the observed spread of the p_x phase-space component.

For the reverse shock, the estimate leading to Equation (6) would also indicate acceleration by $\delta p_x \simeq 0.9\, m_e\, c$ because its Alfvénic Mach number does not significantly differ from that of the forward shock. The more conservative estimate based on beam energy conversion (Equation (7)) suggests $\delta p_x \simeq 0.03\, m_e\, c$, which is three times the spread in p_x or p_y that is assumed near $x = 4900\ \lambda_{se}$ according to Figure 5. Note that the wavelength of the Buneman modes at the foot of the reverse shock is a small multiple of the grid scale, and so the smoothing and coarse pixelization used to produce Figure 4 render the waves invisible in the E_x or density distribution. A Fourier analysis of E_x in the region [4800 λ_{se}; 4900 λ_{se}] reveals a broad peak corresponding to a parallel mode with $k_\parallel\, \lambda_{se} \approx 3 \ldots 7$. The local electron skin length is λ_{se}, and the resonance condition yields, in analogy to Equation (3), a range of relative velocities, $v_{\rm rel} = 0.15\, c \ldots 0.3\, c$. Figure 4 suggest that there are actually 2 streams of ions that propagate relative to the electrons, one with 0.15 c and the other with 0.25 c. We conclude that the broad bump in the Fourier spectrum indicates the presence of two separately excited modes that we cannot individually resolve.

At the two shocks, we can also see a density and magnetic overshoot, i.e., the compression at the shock front with $n_{\rm ov}/n_{\rm up} \approx 8$ surpasses the expected magnetohydrodynamic compression ratio of ~4. The rms amplitude of the magnetic field is about 8.5 times that in the far-upstream region. Such overshoots are common, have been known for a long time, and result from the flux of returning shock-reflected ions, (e.g., Leroy 1983). The modest adiabatic heating associated with this excess compression is marginal compared to the heating that the electrons experience at the shock ramp where an oblique compressive wave mode is evident. We will discuss these waves together with a full account of particle acceleration for the final state of the simulation at $t\Omega_i = 20$.

3.2. Late-stage Evolution

We let our perpendicular shock simulation run for 20 Ω_i^{-1}. Figure 6 presents evidence of the very clear separation of the three discontinuities. The shocks are located at around $x \approx 6750\ \lambda_{se}$ (forward shock) and $x \approx 2800\ \lambda_{se}$ (reverse shock). The shock speeds measured in the simulation frame are consistent with the expected values of $v_{\rm sh,R} = 0.036\, c$ for the forward shock and $v_{\rm sh,L} = -0.093\, c$ for the reverse shock. The CD has reached a position at $x \approx 3850\ \lambda_{se}$, consistent with its predicted speed of $v_{\rm CD} = -0.06\, c$.

From Figure 6, it should be noted that downstream of the overshoot regions, the compression ratio at the shocks is in very good agreement with the hydrodynamical jump conditions for non-relativistic gas with $\Gamma = 5/3$, which predict $n_{R,d}/n_{R,u} = 3.86$ and $n_{L,d}/n_{L,u} = 4.02$ in the simulation frame

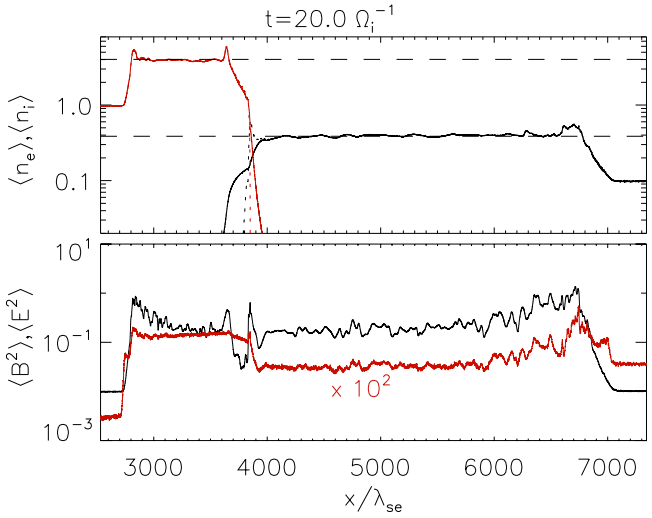

Figure 6. Structure of the collision region at the end of the simulation at time $t = 20\ \Omega_i^{-1}$. Shown in the top panel are the profiles of the average particle-number density, compared with horizontal long-dashed lines marking the expected compression level of $n_{R,d}/n_{R,u} = 3.86$ for the forward shock (lower line) and $n_{L,d}/n_{L,u} = 4.02$ for the reverse shock (upper line). In the bottom panel, we display the average magnetic energy density in black and the electric energy density in red, the latter scaled with a factor 100.

for the forward and reverse shocks, respectively (upper and lower dashed lines in the top panel of Figure 6). We therefore can expect that the system has reached statistical equilibrium for the bulk of the plasma, and a detailed analysis of the shock structure, shock reformation, and particle acceleration can be conducted. We will discuss the two shocks in turn.

3.2.1. Structure of the Forward Shock

Figures 7 and 8 present the structure of the forward shock at the end of the simulation at time $t = 20\ \Omega_i^{-1}$. Displayed in Figure 7 are the density distribution of the electrons and the amplitudes of two components of the electric field and the magnetic field. The distribution of the ions (not shown) closely follows that of the electrons, except where the latter is modulated by the Buneman instability. Figure 8 presents the phase-space distribution of the electrons and ions.

While strong Buneman-type turbulence can be seen directly in the E_x and density distributions around $x = 6950\ \lambda_{se}$ (see Figure 7), a weaker electrostatic mode is seen throughout the precursor, as well as filamentation. The complexity of the turbulence in the precursor region is demonstrated in Figure 9 where we show 2D power spectra of the electron density, the electric field component E_x, and the magnetic field component B_z. The main Buneman modes have $k_\parallel\, \lambda_{se} \simeq 0.8$ (Figure 7(b)), as predicted in Equation (3), and can be slightly oblique (Lampe et al. 1974). The associated density fluctuations are seen only at slightly larger $k_\parallel$ and for small $k_\perp$ (Figure 7(a)). The second mode in the E_x power spectrum, located at $(k_\parallel\, \lambda_{se},\ k_\perp\, \lambda_{se}) \approx (0.25,\ 0.4)$, has no counterpart in the density spectrum, but is also weakly seen in the spectra of other electric or magnetic field components.

The filamentation mode in the precursor is seen in B_z (and also in B_y) at $k_\perp\, \lambda_{se} \approx 0.25$ (Figure 7(c)), equivalent to a wavelength of $\lambda \approx 8\ \lambda_{se,local}$, which corresponds to the separation of current filaments. In the density spectra, however, we see two other peaks at $\lambda \approx 2\ \lambda_{se,local}$ and $\lambda \approx 4\ \lambda_{se,local}$, which are the dominant first two harmonics needed to represent

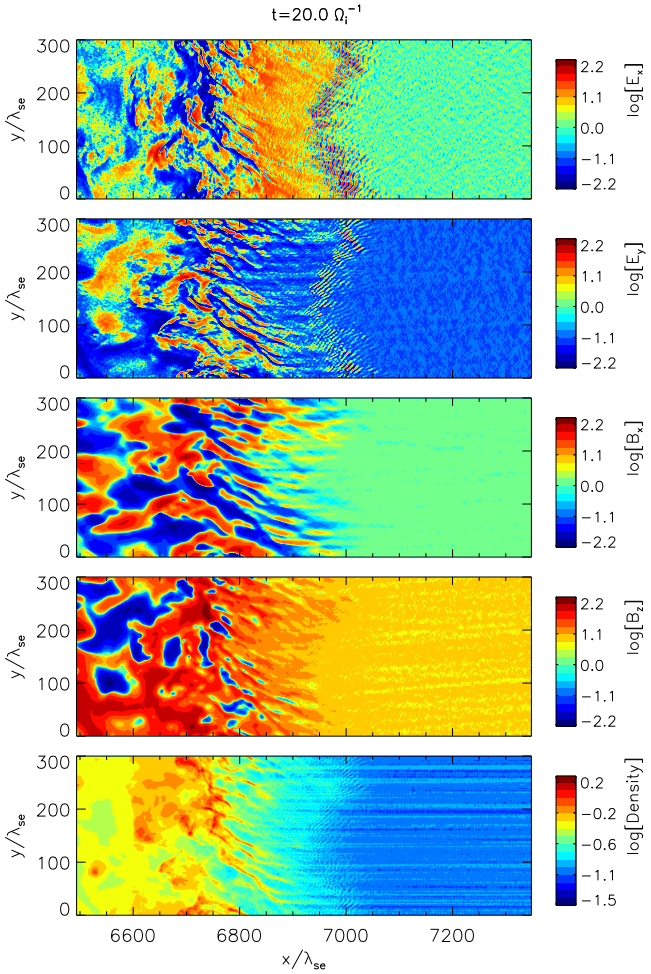

Figure 7. Structure of the forward shock at the end of the simulation at time $t = 20\,\Omega_{\rm i}^{-1}$. Shown from top to bottom are the field components E_x, E_y, B_x, and B_z, followed by the electron density. As in earlier plots, we use a sign-preserving logarithmic scale for the field amplitudes.

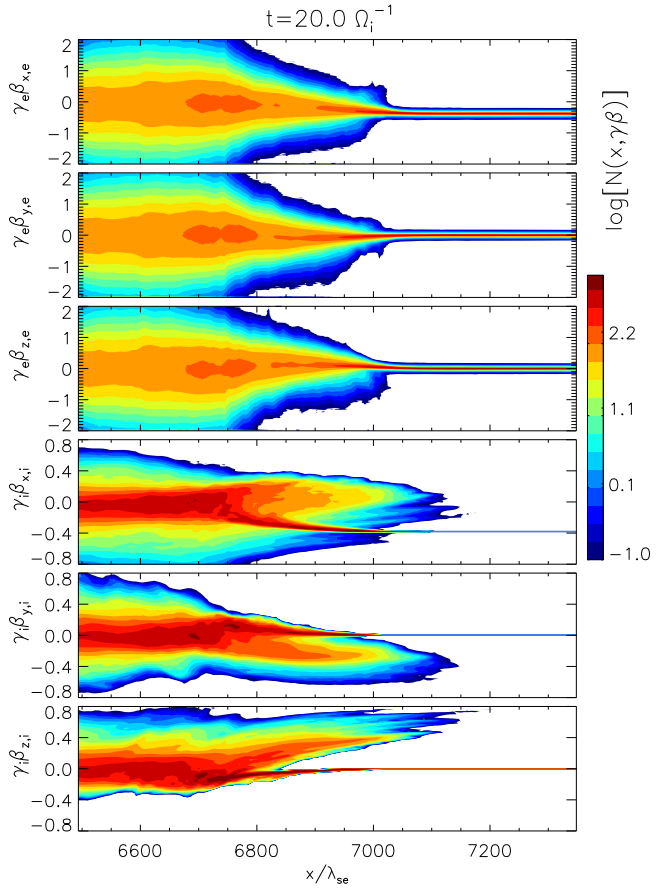

Figure 8. Phase-space distribution near the forward shock at the end of the simulation.

the size of the current filaments, which we estimate as $\sim 3\ \lambda_{\rm se,local}$.

Overall, the amplitude of the waves in the precursor is low and does not increase the field energy density. It is sufficient, however, to keep the electrons warm. Figure 10 displays as a function of the x-coordinate the y averages of the moments of the electron and ion phase-space distributions, the electric field, and the $\boldsymbol{E} \times \boldsymbol{B}$ drift. The normalized electron momentum spread is nearly constant at $p_{\rm rms} \simeq 0.02\,mc$ throughout the precursor, which is about a factor of 10 larger than at injection. We cannot exclude that some of the heating is related to turbulence caused by penetrating or reflected particles from the initial plasma collision.

Further heating can occur at the foot of the shock. Note that the Alfvénic Mach number is too large, or the mass ratio between ions and electron too small, for whistler waves to be generated in the foot region (Matsukiyo & Scholer 2006), which in low-Mach-number simulations were observed to energize electrons (Riquelme & Spitkovsky 2011).

In the shock ramp and further downstream, the electric field shows large fluctuations. Similar variations are seen in the magnetic field, but after smoothing over scales smaller than the electron Larmor radius the $\boldsymbol{E} \times \boldsymbol{B}$ drift speed already has a rather smooth distribution. The shock ramp is clearly delineated by the gradient in $(E \times B)_x$ between $x \simeq 6800\ \lambda_{\rm se}$ and $x \simeq 7000\ \lambda_{\rm se}$, as shown in Figure 10. Over the entire shock ramp, $\boldsymbol{E} \times \boldsymbol{B}$ drift with $v/c \lesssim 0.1$ should occur in the positive z and negative y directions.

A gradient drift is also expected and should lead to shock-drift acceleration (SDA hereafter; Krauss-Varban et al. 1989; Krauss-Varban & Wu 1989). It is important to note, though, that our strictly perpendicular shocks are superluminal, and hence a de-Hoffman–Teller frame does not exist, and injection into SDA should be suppressed (Ball & Melrose 2001).

In the literature, one usually finds the gradient drift discussed in the context of a smooth gradient in the large-scale magnetic field. Written in the downstream frame, i.e., the CD frame, the global gradient of the magnetic field near a nonrelativistic shock front causes a particle of mass m and charge q to drift with a velocity of (e.g., Guo et al. 2014)

$$v_{\rm gd} = \frac{p_\perp^2}{2\,m\,q\,B}\,\frac{\boldsymbol{B} \times \boldsymbol{\nabla} B}{B^2} = \frac{{\rm sgn}(q) p_\perp^2}{2\,m\,m_{\rm i}\,\Omega_{\rm i}}\,\frac{\boldsymbol{B} \times \boldsymbol{\nabla} B}{B^2}, \quad (8)$$

where $p_\perp$ is the momentum perpendicular to the magnetic field. The first point to note is the dependence on the charge sign, ${\rm sgn}(q)$, which mandates that electrons and ions drift in opposite directions. The second fraction on the right-hand side of Equation (8) must, on average, be similar to the inverse thickness of the shock ramp, $\sim \Omega_{\rm i}/v_{\rm sh}$. Furthermore, noting that momentum

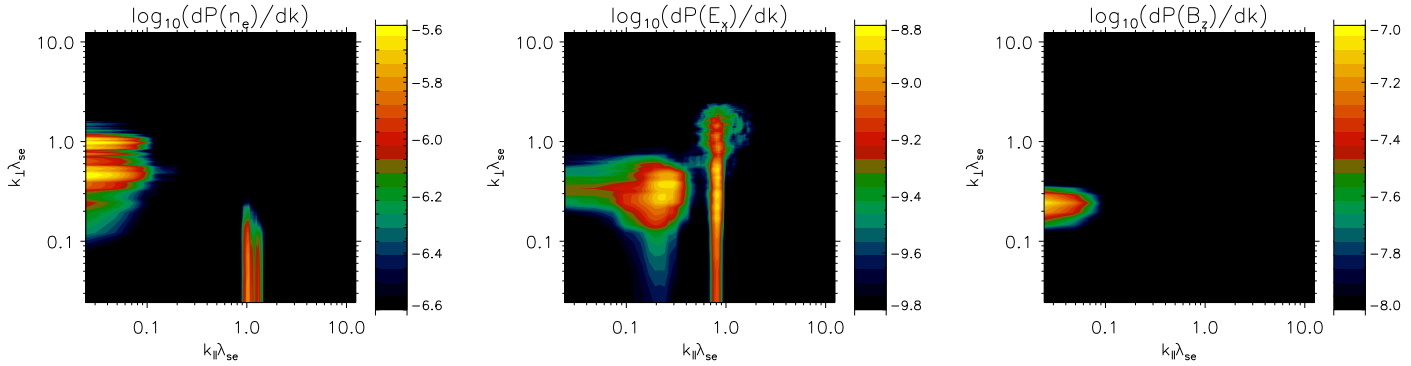

Figure 9. Fourier power spectra taken in the region 7100 λ_{se}–7360 λ_{se}. Shown in 2D reduced wavevector space $(Z_{\parallel}, Z_{\perp}) = (k_{\parallel}\,\lambda_{se}, k_{\perp}\,\lambda_{se})$ are spectra of the electron density (left), the electric field component E_x (middle), and the magnetic field component B_z (right).

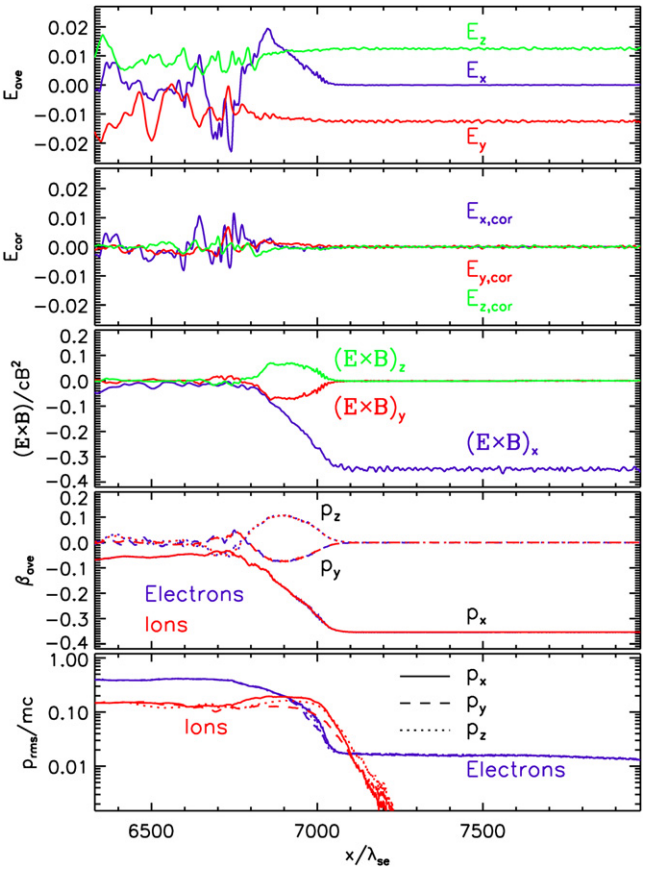

Figure 10. Moments of the phase-space distribution of electrons and ions in comparison to the electric field components in the simulation frame and in the local flow frame given by β_{ave}, and the components of $\boldsymbol{E} \times \boldsymbol{B}$ drift. All quantities are averaged over the y-coordinate. For ease of comparison with the drift speed, we plot the average motion as velocity $\beta = p/mc(1 + p^2)$.

conservation on average requires $p_{\perp}^2 \simeq (3/8)m^2\, v_{sh}^2$, Equation (8) can be simplified to

$$|v_{gd}| \lesssim \frac{3}{16}\,\frac{m}{m_i}\,v_{sh} \simeq 0.075\,c\,\frac{m}{m_i}, \qquad (9)$$

or about 0.05 c projected along the y and z axes, indicating that, whereas the ions may drift with a velocity not much smaller than that of $\boldsymbol{E} \times \boldsymbol{B}$ drift, electrons would be considerably slower.

Standard descriptions of SDA, including the lack of injection into it at superluminal shocks, rely on the concept of a smooth shock transition in which the magnetic field gradient is a clearly discernible feature. One consequence of this is that gradient drift should exist, but here it does not. Turbulence in the ramp destroys this picture, and the true electromagnetic environment likely deviates from the simple concept, as demonstrated, e.g., on page 6 of Matsumoto et al. (2012) and attributed there to the time dependence arising from shock reformation. The large fluctuations in the electric and magnetic fields in the shock ramp play havoc with the gradient drift because small- and medium-scale structures provide a far more dominant contribution to ∇B. We could not find an averaging scheme that permits extracting from the simulation data a gradient drift corresponding to that calculated for the globally expected compression of the large-scale magnetic field.

The observed mean velocity, $\boldsymbol{\beta}_{ave} = \boldsymbol{v}_{ave}/c$, follows closely that expected from $\boldsymbol{E} \times \boldsymbol{B}$ drift. There is no discernible difference in the flow of electrons and ions, indicating the absence of a significant gradient drift. Note that $\boldsymbol{E} \times \boldsymbol{B}$ drift is not a property of the reflected particles alone. The average particle velocity corresponds to the drift speed, implying that reflected particles have transverse speeds a factor of a few higher than the drift speed.

We can transform the electric field into the local flow frame given by $\boldsymbol{\beta}_{ave}$. The resulting field in this guiding-center frame, $\boldsymbol{E}_{cor}$, is displayed in the second panel of Figure 10; note the low amplitude throughout the shock ramp. We emphasize the important lesson that the existence of an electric field component parallel to the drift direction of the particles does not imply the existence of a significant electric field in the drift frame.

Plasma crosses the ramp in a time $t_{rc} \simeq \Omega_i^{-1}$. For individual ions, the separation of motion into drift and gyration is thus questionable, whereas for electrons a guiding-center approximation should work well. Averaged over their Larmor motion, electrons see only very weak electric fields, and hence are not significantly accelerated beyond the adiabatic compression at the shock unless their Larmor radius is of the same order or larger than the ramp thickness on account of pre-acceleration at the foot or further upstream. Ions generally fulfill that condition, and so they may see a coherent electric field along their trajectory across the ramp and be accelerated.

The ion distribution in the ramp is composed of incoming, reflected, and returning reflected particles whose superposition may provide a reasonable sampling of the gyrophase, thus

retaining the crude but still reasonable guiding-center approximation for $\boldsymbol{E} \times \boldsymbol{B}$ drift, and hence the agreement between the expected and observed drift speeds. The significant increase in $p_{\rm rms}$ of the ions at the foot of the shock between $x = 7000\ \lambda_{\rm se}$ and $x \simeq 7100\ \lambda_{\rm se}$ does not indicate heating but reflects the momentum offset between incoming and reflected particles. A similar effect is expected for electrons, but would not be as easily identifiable on account of their small Larmor radius.

In Section 3.3, we will discuss in detail the resulting particle spectra in the downstream region. Here, we only note that the normalized moment spread, $p_{\rm rms}/mc$, of electrons in the far downstream region evolves to about four times that of the ions. The ratio of electron temperature to that of ions, if thus defined, is then

$$\frac{T_{\rm e}}{T_{\rm i}} \simeq 0.28, \tag{10}$$

which is much larger than the $1/50$ expected for purely magnetic isotropization, but still short of equilibration. Observationally, one finds with few exceptions a correlation of $T_{\rm e}/T_{\rm i} \propto v_{\rm sh}^{-2}$ (for a review see Ghavamian et al. 2013). A conceptual explanation for this empirical relation lies in electron heating through turbulence generated by reflected ions whose number depends on the shock speed. It is not easy to relate the temperature relation found in our simulation to those inferred for real SNRs because we use a reduced mass ratio and the empirical relation does not distinguish between the different efficiency in ion reflection for the perpendicular and parallel shocks.

The Buneman modes excited at the shock foot may give rise to SSA of electrons (Leroy et al. 1981; Amano & Hoshino 2009b; Matsumoto et al. 2012). Despite the electron heating in the far-upstream region, the high sonic Mach number of the shock exceeds the threshold for the growth of Buneman modes (see Equation (4)) as the first stage of electron acceleration. Visual inspection of Figure 7 reveals the non-planarity of the foot region, i.e., rippling (see Section 3.2.2). We therefore select a small region ($6970\ \lambda_{\rm se} < x < 7050\ \lambda_{\rm se}$ and $y \leqslant 125\ \lambda_{\rm se}$) for further analysis that appears to harbor a planar sheet of strong electrostatic fluctuations. Figure 11 displays a Fourier spectrum of the electric field parallel to the wave vector, $\boldsymbol{e}_k \cdot \boldsymbol{E}$. We observe a strong signal at $k_\parallel\ \lambda_{\rm se} \simeq 0.7$, as has already been seen during the early evolution and is in fact expected (see Equation (3)). This is clearly a Buneman mode and not an ion-acoustic wave, which would have a much larger wavenumber, k. Matsumoto et al. (2012) conducted 2D PIC simulations of non-relativistic shocks with Alfvénic Mach numbers and ion/electron mass ratios similar to those in our work. They find an electrostatic mode with $k_\perp/k_\parallel \simeq 0.5$, whereas in our simulation $k_\perp/k_\parallel \simeq 0.15$ (and slightly larger than that for regions shifted along the transverse coordinate, y). The linear analysis of Amano & Hoshino (2009a) suggests that oblique modes should be strong for electron–ion drift that is much faster than the electron thermal velocity, whereas the parallel mode should dominate right above the threshold of the instability. Indeed, a Fourier spectrum taken further upstream (for $x > 7050\ \lambda_{\rm se}$) shows a prominent oblique mode, albeit with an intensity a factor of 10 lower than that observed right at the foot.

It is instructive to compare the v_x–v_y ion phase-space density distribution in our simulation data to that of Matsumoto et al.

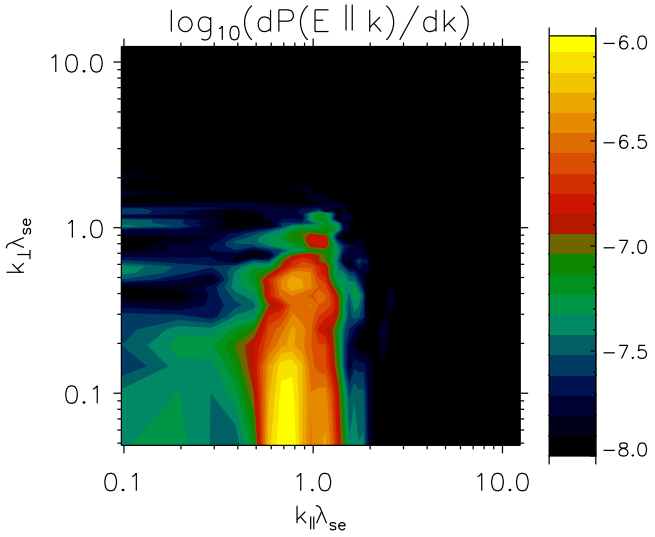

Figure 11. Fourier power spectrum of the electric field parallel to the wave vector, $\boldsymbol{e}_k \cdot \boldsymbol{E}$, in the region $6970\ \lambda_{\rm se} < x < 7050\ \lambda_{\rm se}$ and $y \leqslant 125\ \lambda_{\rm se}$.

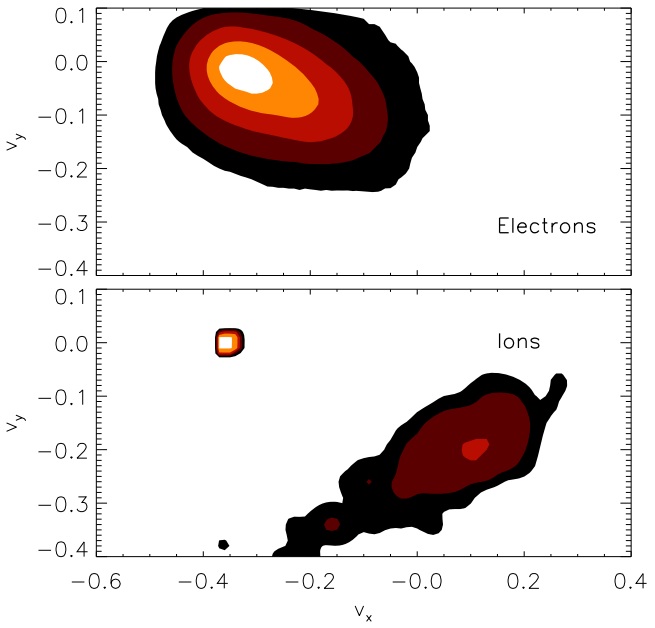

Figure 12. Phase-space distribution in v_x–v_y of electrons (Top panel) and ions (Bottom) in the section of the foot region from which we extracted the Fourier spectrum shown in Figure 11. The scale is logarithmic with maximum at 40% of the peak density. The dynamic range is 33,000 for electrons and 230,000 for ions.

(2012, see their Figure 2(a)) and Matsumoto et al. (2013). In the region where Buneman modes are strong, they find reflected ions with substantial v_y on the order of the shock speed. Figure 12 displays the phase-space distribution in our simulation, and it is evident that the drift speed between electrons and ions is oriented in various directions. The density peak in the distribution of reflected ions corresponds to approximately $v_y/v_x \simeq 0.3$, which is in fact the only drift component that is also seen a bit further upstream, indicating that an instability driven by this component was already operating in those regions, and thus may have reached a large amplitude.

The main difference between our simulation setup and that of Matsumoto et al. (2012, 2013) is that they assume the large-

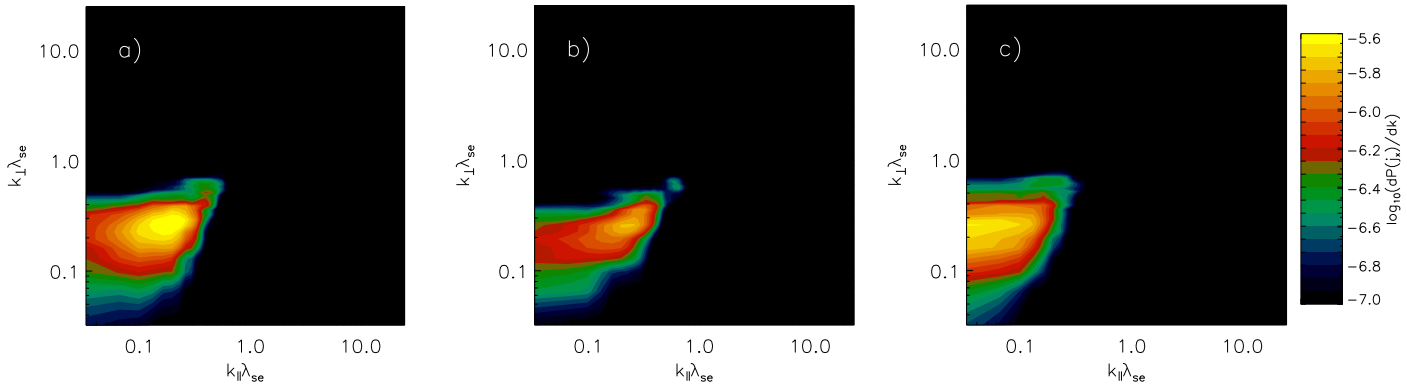

Figure 13. Fourier spectra of the current density in the x-direction, $\boldsymbol{j}_x$, in the ramp region 6760 $\lambda_{se} < x <$ 6960 λ_{se}. Panel (a) on the left displays the spectrum for nominal coordinates x and y, whereas for panels (b) and (c) the y coordinates were shifted before computing the Fourier spectrum. For panel (b), we compensated the average velocity of all ions (see Figure 10), whereas for panel (c) on the right we compensated only the average motion of incoming ions.

scale magnetic field to be strictly out of plane and their electron plasma beta is close to unity, whereas for us it is on the order of $1/25$ even after electron heating in the far-upstream region. Accounting for magnetic field orientation yields a factor of $\sqrt{2}$, as only $1/\sqrt{2} \simeq 0.71$ of the large-scale magnetic deflection projects on the y-axis, and we still find both the direction of the reflected ions and the wave vector of the Buneman modes aligned closer to the shock normal than is the case in the simulation of Matsumoto et al. (2012). As it is unclear how the plasma beta could cause this discrepancy, its origin remains unclear. In general, the non-Maxwellian form of the particle distribution functions and their rapid change in the foot and ramp regions renders difficult a linear analysis of wave types and instabilities.

In the ramp region, a nearly perpendicular electromagnetic mode is evident in the field components shown in Figure 7. Similar filaments were observed in the foot region in the simulation of Kato & Takabe (2010) and identified as current filaments resulting from the Weibel-type instabilities that were shown to mediate high-speed nonrelativistic unmagnetized and weakly mangetized parallel shocks (Kato & Takabe 2008; Niemiec et al. 2012). We conducted a Fourier analysis and indeed found strong evidence of filamentation in $\boldsymbol{j}_x$ and $\boldsymbol{j}_z$ (out of plane) that is largely carried by incoming particles. Figure 13 compares the Fourier spectra of $\boldsymbol{j}_x$ that were computed for nominal coordinates x and y with those calculated after shifting the y coordinates to compensate for the curved large-scale trajectories of the plasma. We find a nearly perpendicular mode, indicating straight current filaments, only when accounting for the average velocity of the incoming ions alone (Figure 13(c)). The wavelength is about two local ion skin lengths, $\lambda \approx 2\ \lambda_{si,loc}$, with the main uncertainty arising from averaging the local skin length over the density gradient in the shock ramp. Equally strong perpendicular fluctuations are seen in $\boldsymbol{j}_z$, extending in wavelength to $\lambda \approx 4\ \lambda_{si,loc}$. The Fourier signal in $\boldsymbol{j}_y$ shows a peak at similar scales, but is weaker. If we separately consider the current density carried by electrons and that of ions, then we find large Fourier amplitudes for perpendicular scales larger than $2\ \lambda_{si,loc}$ that seem to compensate for each other, suggesting a density structure that is more complex than that seen in $\boldsymbol{j}_x$.

We do not see any evidence for spontaneous turbulent reconnection in the ramp, which was recently reported by Matsumoto et al. (2015). They noted a chain of magnetic islands coinciding with spikes in electron density resembling structures seen in dedicated simulations of turbulent reconnection. There, the neutral lines appear to break up into contracting magnetic islands in which trapped electrons are accelerated through a Fermi-like process (Drake et al. 2006). The filaments in our simulations are only weakly modulated on a scale similar to that of the Buneman waves in the foot, which the electrons passed through on their way up the ramp. Further modulation arises from filament mergers, but the amplitudes are moderate and they also do not align into a chain of magnetic islands.

3.2.2. Structure of the Reverse Shock

Figure 14 presents the structure of the reverse shock at the end of the simulation at time $t = 20\ \Omega_i^{-1}$. Displayed are the density of the electrons and the amplitudes of four components of the electromagnetic field. In terms of the shock parameters, the main difference from the forward shock is a significantly lower sonic Mach number, $M_s = 252$ instead of $M_s = 755$. Both the shock speed and the skin lengths are smaller by about a factor of three compared to their values at the forward shock, and so the reverse shock extends over fewer grid points and is not as well resolved by the simulation.

In Figure 14, note that the shock surface is highly perturbed, and these shock-front fluctuations can be identified as ripples. They occur on spatial scales of about $150\ \lambda_{se} \approx 20\ \lambda_{si}$ and are visible through correlated fluctuations in density and all electromagnetic field components. Time analysis reveals that the ripples propagate in the $+y$-direction with an average speed of $0.08\ c \approx 18\ v_{A,L}$. Their structure is highly dynamic on timescales as short as $0.1\ \Omega_i^{-1}$ and their shape changes, typically toward an asymmetric wave pattern. The amplitude of rippling, i.e., the displacement in x, varies between $2\lambda_{si}$ and $5\lambda_{si}$. The ripples emerge with small amplitude at the same time as the shock itself ($t\Omega_i = 4$–5), and they may initially be influenced by the curved structure of the CD resulting from an incoherent development of filamentation instabilities on both sides of the discontinuity (see Figure 2). The subsequent evolution is highly variable in amplitude and wavelength (100–300 λ_{se}). The specific form of the ripples shown in Figure 14 is acquired only during late-stage evolution at $t\Omega_i \approx 16$.

Shock rippling is known from numerical studies of quasi-perpendicular super-critical low-Mach-number shocks performed in two or three dimensions with transverse sizes large enough to contain several ion skin lengths (see, e.g., Winske &

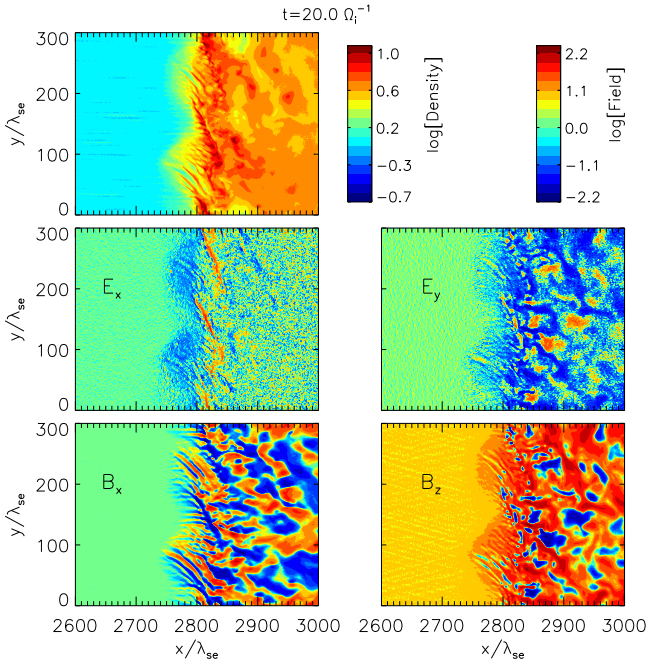

Figure 14. Structure of the reverse shock at the end of the simulation. Shown are, with proper aspect ratio, the electron density in the top left and the field components E_x, E_y, B_x, and B_z. As in earlier plots, we use a common sign-preserving logarithmic scale for the field amplitudes, displayed in the upper right corner.

Quest 1988; Thomas 1989; Lowe & Burgess 2003; Burgess & Scholer 2007; Umeda et al. 2009, 2010, 2014). The ion temperature anisotropy arising from ion reflection at the shock can drive the Alfvén ion cyclotron (AIC) or the mirror instability in the shock ramp, and the resulting unstable modes have wavelengths of *a few* ion skin depths and propagate along the regular magnetic field, significantly contributing to ion isotropization and thermalization at the shock and downstream. Studies of such wave structures with 2D simulations require the in-plane configuration of the magnetic field. For out-of-plane field configurations, which suppress parallel-propagating waves, Burgess & Scholer (2007) demonstrated the existence of another shock-front instability that produces fluctuations on a spatial scale commensurate with the gyroradius of shock-reflected ions, which propagate along the shock surface with the speed and direction of the ions gyrating in the shock foot. They showed that the instability requires sufficiently high Alfvénic Mach numbers, M_A, but which are still in the range considered here as the low-Mach-number regime, or low plasma beta, and can also occur for magnetic field orientations of $\phi \neq 90°$. Although our simulation with $\phi = 45°$ allows both types of instabilities to develop in the system, the characteristics of the observed ripples agree with the scenario of Burgess & Scholer (2007), i.e., a modulation of shock-reflected ions along the shock surface. The wavelength of the ripples, 150 λ_{se}, is approximately equal to the gyroradius of the reflected ions in the upstream magnetic field projected on the y-axis. Their propagation speed and direction is also in agreement with the reflected-ion speed projected onto the shock surface, for which we find 0.07–0.09 c in an analysis of the ion phase-space distribution in the shock foot. Modes driven by ion temperature anisotropy are not excited because plasma isotropization at the shock is effected by Weibel-like filamentation instabilities, and electrons are already relativistically hot through interactions with Buneman waves at the shock foot.

We note that the rippled shock structure can at some times also be observed at the forward shock (e.g., Figure 7). The amplitude of the ripples is similar to that in the reverse shock in terms of the local plasma skin depth. Shock surface fluctuations now move in the $-y$-direction, consistent with the opposite sense of rotation of the reflected-ion rotation due to the opposite plasma inflow velocity (Burgess & Scholer 2007). We thus conclude that the mechanism of ripple formation is the same as at the reverse shock. However, the gyroradius of ions reflected at the forward shock is in the range of 120–200 $\lambda_{se,R}$ = 380–630 λ_{se}, which is larger than the transverse size of our computational box. The development of the ripples at the forward shock is therefore influenced by our boundary conditions.

Shock-front ripples have not yet been reported in multi-dimensional studies of high-Mach-number perpendicular shocks. Two-dimensional studies in out-of-plane magnetic field geometry (Matsumoto et al. 2012, 2013) suppress AIC waves and typically use computational boxes with transverse size of 5–6 λ_{si} that cannot contain ion-gyroscale modulations. Ion-scale ripple structures have not been identified in the large-scale ($L_y \sim 36.5\ \lambda_{si}$) 2D simulations of Kato & Takabe (2010) with in-plane magnetic field configuration, although a visual similarity was noted for the magnetic field and density patterns at and behind the overshoot to the structures reported in Winske & Quest (1988). The results of our simulation with a magnetic field inclined at $\phi = 45°$ to the simulation plane are thus in agreement with these earlier studies, and they also suggest that rippling at the gyroscale of ions will significantly contribute to shock-front nonstationarity even in 3D simulations.

As a consequence of the rippled structure, the reflection rate of the ions is enhanced at some locations along the shock front, which is clearly visible through the modulated extension of the filaments in the foot. These regions then provide stronger Buneman instability which should lead to more efficient localized electron heating and acceleration (see Umeda et al. 2009 for similar effects in low-Mach-number shocks). Due to the poorly resolved foot structure at the reverse shock, a detailed analysis of this possible connection between shock ripples and electron energization must be deferred to future work.

Figure 15 displays moments of the phase-space distributions of particles near the reverse shocks. Note that the particle drift along the shock surface is well described as $\boldsymbol{E} \times \boldsymbol{B}$ drift, as is the case of the forward shock, and likewise the electric field is of very low amplitude in the guiding-center frame. Gradient drift is a prerequisite of SDA but seems to play a negligible role in the dynamics of electrons and ions.

Fourier spectra of the electron density in the upstream region taken from the region 2660 λ_{se}–2725 λ_{se} indicate a mode at $k_\perp\ \lambda_{se} \approx 0.8$ and nothing else. A corresponding signal is seen in B_z at $k_\perp\ \lambda_{se} \approx 0.6$. The same perpendicular mode was observed upstream of the forward shock (see Figure 9), albeit at slightly smaller scales. The parallel mode observed at the fast shock is absent ahead of the slower shock, at least in the electron density. In E_x, we see a parallel mode at $k_\parallel\ \lambda_{se} \approx 6$ and an oblique mode similar to that visible in Figure 9, but at twice the wavenumber. Assuming that the parallel mode in E_x is a Buneman wave, we can use Equation (3) to infer the drift

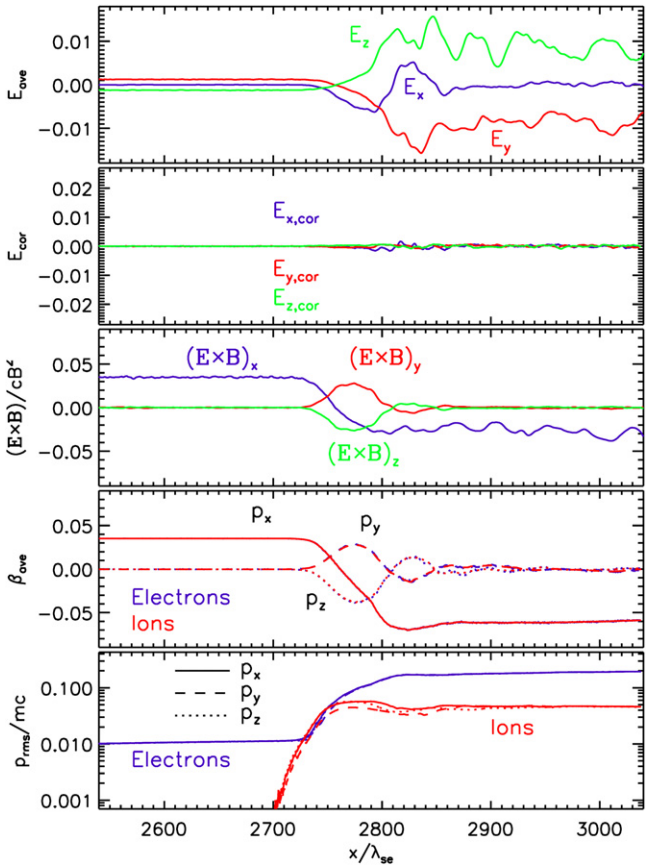

Figure 15. Moments of the phase-space distribution of electrons and ions comparison with the electric field components, both in the simulation frame and in the guiding-center frame, and the components of $\boldsymbol{E} \times \boldsymbol{B}$ drift in the region around the reverse shock. All quantities are averaged over the y-coordinate. For ease of comparison with the drift speed, we plot the average motion as velocity $\beta = p/mc(1 + p^2)$.

velocity between electrons and ions to be $v_{\rm rel} \simeq 0.16\,c$, which corresponds to 30% more than the shock speed, which is about the expected value.

The Buneman mode is very weak far upstream but, in fact, dominates the Fourier spectrum of $E_\parallel = \boldsymbol{E} \cdot \boldsymbol{e}_k$ in the foot region. We have to select small regions for further analysis on account of the large amplitude of shock rippling. For example, in the region $2720\ \lambda_{\rm se} \leqslant x \leqslant 2760\ \lambda_{\rm se}$ and $y \leqslant 40\ \lambda_{\rm se}$, we see a strong signal in $E_\parallel = \boldsymbol{E} \cdot \boldsymbol{e}_k$ at $k_\parallel\ \lambda_{\rm se} \approx 6$ and $k_\perp\ \lambda_{\rm se} \leqslant 3$. The phase-space distribution of particles in the same region indicates a drift of reflected ions relative to the electrons with $\boldsymbol{v}_{\rm rel} \simeq (-0.14\,c,\ 0.07\,c)$, and so the relative speed is indeed $0.15\,c$ and the electrostatic mode can be identified as a Buneman wave.

Throughout the ramp, we observe filaments in $\boldsymbol{j}$ with corresponding filamentary structure in the components of the magnetic field. Our analysis of the forward shock demonstrated that the current filaments are carried by incoming particles and are bent according to their deflection in the ramp region. Qualitatively, we see the same at the reverse shock. It is difficult to establish a quantitative match, however, because the strong shock rippling imposes significant variations in the local flow velocity of incoming particles. Overall, the main structural differences between the forward and reverse shocks are caused by the existence of rippling, which are only fully resolved here for the reverse shock.

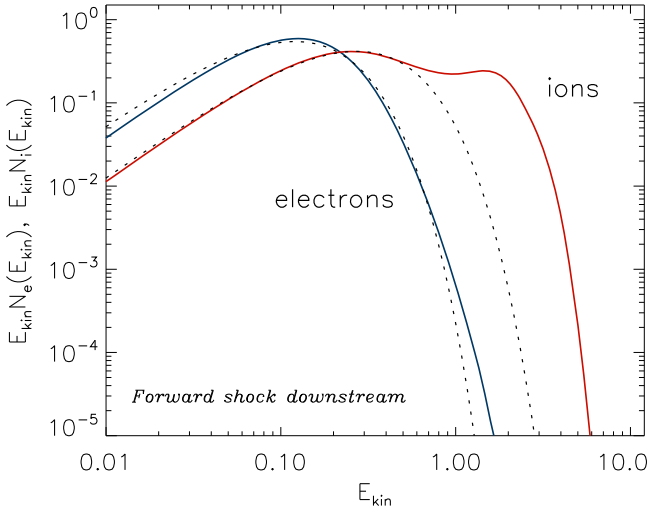

Figure 16. Kinetic-energy spectra of electrons (blue line) and ions (red line) at time $t = 20\,\Omega_{\rm i}^{-1}$ and the region $x \approx 5000$–$5700\ \lambda_{\rm se}$ far downstream of the forward shock at $x \approx 6800\ \lambda_{\rm se}$. The spectra are calculated in the downstream rest frame. They are normalized and expressed in simulation units, in which $m_{\rm e}c^2 = 0.25$. The dotted lines indicate fits of a relativistic Maxwellian.

3.3. Particle Distributions

In a collisionless environment (and in our PIC simulation), isotropization and relaxation to near-Maxwellian distribution functions is achieved through interactions with plasma turbulence (Bret 2015), which can be described as a collision term in the Boltzmann equation (Baalrud et al. 2009, 2010). At collisionless shocks, this turbulent isotropization provides validity to a hydrodynamical description on large scales. High-energy tails in particle spectra may develop at a shock, however, which permits the injection of particles into Fermi-type acceleration processes. Care must be exercised to distinguish true spectral tails from the apparent spectral structure that arises from incomplete isotropization.

Figures 16 and 17 show particle distributions in kinetic energy, $E_{\rm kin} = (\gamma - 1)m_{\rm l}c^2$ ($m_{\rm l} = m_{\rm e}$, $m_{\rm i}$), downstream of the forward and the reverse shock, respectively, at $t = 20\ \Omega_{\rm i}^{-1}$. The spectra are calculated in the downstream rest frame, defined by the CD speed $\beta_{\rm CD} = -0.06$ in the simulation frame. We selected slices in the downstream region of the shocks that are about five ion gyro radii in width considering the shock-compressed field, or about two ion gyro radii for the far-upstream magnetic field, $2\ v_x\ \Omega_{\rm i}^{-1}$. For the forward shock, this implies a separation from the shock by $1100\ \lambda_{\rm se}$, whereas for the reverse shock the distance is only $110\ \lambda_{\rm se}$ on account of the much smaller shock speed. At these locations, the plasma is homogeneous and free of particles that penetrated the contact discontinuity. In the CD rest frame, both ion and electron distributions are isotropic and display no large-scale bulk motion.

For both the forward and the reverse shock, the distributions of electrons appear to be quasithermalized and well reproduced by relativistic Maxwellians. A Maxwellian fit to the bulk of the ion distributions suggests a temperature ratio of $T_{\rm i}/T_{\rm e} \approx 2$. In addition, the ion spectra exhibit a significant supra-thermal tail. With the exception of electrons downstream of the reverse shock, whose temperature slightly increases with distance from the shock, particle spectra do not show significant evolution. Their distributions at fixed distance from the shock are also

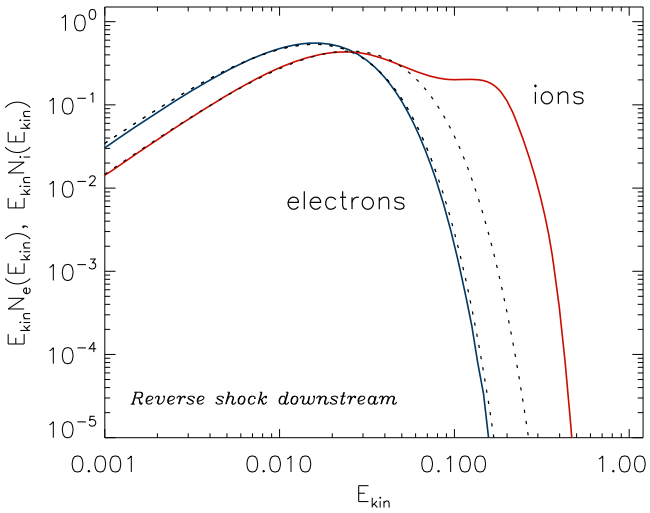

Figure 17. Kinetic-energy spectra of electrons (blue line) and ions (red line) at time $t = 20\ \Omega_i^{-1}$ and in the region $x \approx 2910$–$2980\ \lambda_{se}$ far downstream of the reverse shock at $x \approx 2800\ \lambda_{se}$. The spectra are calculated in the downstream rest frame. They are normalized and expressed in simulation units in which $m_e c^2 = 0.25$. The dotted lines indicate relativistic Maxwellian fits.

approximately steady in the time for $t \approx 5$–$20\ \Omega_i^{-1}$, which demonstrates that the system has attained a quasi-equilibrium within the runtime of our simulations.

It is well known that the formation of supra-thermal tails in the ion distribution at perpendicular shocks can result from SSA in which shock-reflected particles performing half of a gyro cycle upstream increase their energies through motion along the convective electric field. The maximum ion energy is roughly constant in our simulation, which suggests that a typical particle needs only a few gyro cycles to traverse the shock potential and be transmitted downstream. The pre-accelerated ions may be subject to further energization by DSA, a process that operates on larger scales than are covered in our simulations. However, recent hybrid simulations suggest a low DSA efficiency for perpendicular shocks (Caprioli & Spitkovsky 2014).

The downstream electron distributions show either no (reverse shocks) or only marginal (forward shock) non-thermal populations. This is in contrast to the results of Matsumoto et al. (2012) for their Runs A and C using parameters similar to ours; in particular, a quite low plasma beta β_p where efficient acceleration by an electron SSA process was observed. This process requires nonlinear growth of the Buneman modes in the shock foot. Electrons in this region can be trapped in coherent electrostatic potential structures and be directly accelerated by the convective electric field. They eventually escape from the potential wells and start to drift downstream. However, if a particle gains enough energy at the first encounter with the Buneman waves and its gyroradius increases, it can enter the electrostatic wave region again from the downstream side and experience another SSA cycle (see also Amano & Hoshino 2009b). As shown in Section 3.2, Buneman-type turbulence is generated in the foot in both the forward and the reverse shock, and in the former it grows to nonlinear amplitudes.

During the early evolution of the simulation (see Section 3.1), we have seen that the estimates of electron acceleration efficiency presented in Matsumoto et al. (2012) are too optimistic. It appears that fast electrons violate the trapping condition. Efficient electron heating can occur, as demonstrated in Sections 3.1 and 3.2. However, relativistic particles easily escape the electrostatic potential well and their acceleration is not efficient.

Inefficient production of non-thermal electrons was also reported by Kato & Takabe (2010) in their simulations of an extremely high-Mach-number shock, $M_A \sim 130$. As in the case studied here, shock formation was mediated by a Weibel-like filamentation instability that generated mostly magnetic turbulence. Although an unstable electrostatic mode was found in the foot of the shock and identified as the Buneman wave, the growth of the instability was very slow due to the high temperature of the reflected ions. It is unclear what role is played by filamentation that may prohibit efficient growth of the Buneman waves to strongly nonlinear amplitudes, as we observed similar filaments, as did, e.g., Matsumoto et al. (2013). The turbulent structure of the shock transition may also play an important role in impeding a return of electrons to the foot region or suppressing the SDA of electrons in the shock ramp, which should accompany the electron SSA process (Matsumoto et al. 2012).

Kato & Takabe (2010) attributed the lack of efficient electron acceleration to the specific orientation of the upstream magnetic field in the plane of the simulation, which was different from the out-of-plane configuration assumed in Amano & Hoshino (2009b). The simulations by Matsumoto et al. (2012) and Matsumoto et al. (2013) with out-of-plane magnetic field and moderate plasma beta, $\beta_p = 0.5$, show a high efficiency of electron energization. We observed little electron acceleration for small plasma beta; Matsumoto et al. (2012) observed little electron acceleration for high plasma beta, $\beta_p = 4.5$; and Kato & Takabe (2010) observed little electron acceleration for very high plasma beta, $\beta_p \sim 26$, suggesting that the plasma beta is not the decisive factor.

The ion-to-electron mass ratio used in our study also should *not* play a role. Although the publications by Matsumoto et al. (2012, 2013) are based on a larger m_i/m_e of 100–225, as compared to 30–50 in Kato & Takabe (2010) and this paper, earlier studies by Amano & Hoshino (2009b) and Run A in Matsumoto et al. (2012), with $m_i/m_e = 25$, show effective electron pre-acceleration through the SSA process. Larger ion-to-electron mass ratios lead to higher amplitudes of the magnetic field at the overshoot and, in conditions allowing for efficient electron SSA, enable further acceleration through adiabatic processes at the shock for already relativistic pre-accelerated electron populations (Matsumoto et al. 2012).

The obvious difference between simulations showing efficient electron acceleration and studies yielding little electron energization is the configuration of the regular magnetic field component with respect to the simulation plane. It appears that strong acceleration through SSA is seen when the large-scale magnetic field is assumed to be strictly out of plane, as in Amano & Hoshino (2009b) and Matsumoto et al. (2012, 2013). On the other hand, turbulent reconnection is seen only in a simulation with in-plane magnetic field (Matsumoto et al. 2015). The Buneman modes have wavevectors preferentially aligned with the reflected-ion beam, and thus are better resolved in 2D studies when the ion gyro-motion is contained in the plane of a simulation, i.e., for out-of-plane magnetic field configurations (Riquelme & Spitkovsky 2011). Our simulation with 45° field orientation should well resolve the Buneman instability and enable turbulent reconnection processes, thus

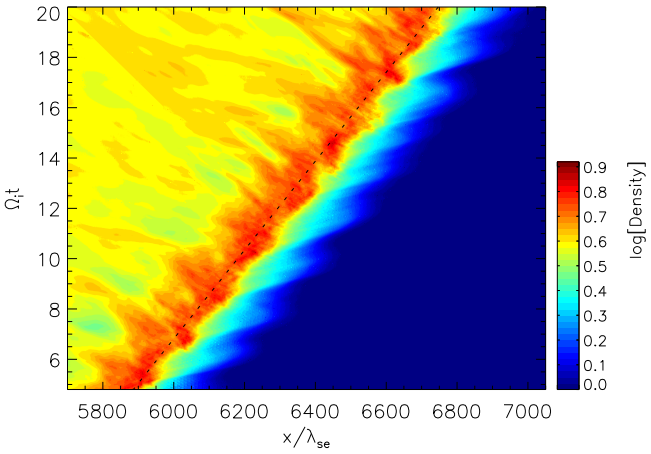

Figure 18. Electron density in the vicinity of the forward shock as a function of position and time, averaged over the y-coordinate. The dashed line marks the mean location of the shock front propagating with $v_{\rm sh,R}$.

allowing 3D physics to be approximated in a 2D simulation. The apparent lack of efficient electron acceleration in our setup may suggest that the efficacy of these kinetic instabilities in three dimensions is lower than in idealized 2D configurations. Fully 3D simulations appear to be required.

3.4. Shock Reformation

Studies of low-Mach-number super-critical perpendicular shocks have demonstrated that the shock front is non stationary and recurrently disappears and re-develops on a timescale of the order of the downstream ion gyroperiod. The process is called a cyclic self-reformation of the shock and is caused by the dynamics of the shock-reflected ions (see, e.g., Treumann 2009; Umeda et al. 2010, 2014).

Figure 18 shows the time evolution of the average density profile in the vicinity of the forward shock. In this representation, the shock moves from left to right with an average speed of $v_{\rm sh,R}$, as marked with the dashed line. Although the shock never completely disappears, a self-similar cyclic evolution of the average profile is evident. Self-repeating reformation phases occur with a period of approximately 1.5 $\Omega_{\rm i}^{-1}$ and are marked by shifts of the shock ramp position with the enhancements in plasma density at the shock, and extensions of the filamentary region in the shock foot.

The shock reformation arises because specular ion reflection from the shock ramp is not a continuous process. As frequently observed in low-Mach-number shocks, reflected ions bunch in the upstream edge of the shock foot due to either a non-steady reflection rate or steepening of plasma waves excited in this region (see, e.g., Umeda et al. 2010) In time, the cross-shock potential builds at this location and a new shock front develops. In our simulation of high-Mach-number shocks, we see similar effects. However, the physics of reflected-ion bunching is now governed by the dynamics of current filaments resulting from the Weibel-like instability that mediates the shock transition.

The main features of a shock-reformation cycle in the forward shock are illustrated in Figure 19 in a series of snapshots displaying distributions of the electron density, the E_x electric field component, and the ion phase space. Our results are displayed in the shock rest frame, and a mean shock ramp position that moves with a constant velocity of the forward shock $v_{\rm sh,R}$ is marked with a dashed vertical line (compare Figure 18). At time $t = 17.1\ \Omega_{\rm i}^{-1}$ (Figure 19(a)), density compressions and associated quasi-regular electric field potential structures are formed approximately 50 $\lambda_{\rm se} \simeq 2\ \lambda_{\rm si,R}$ from the shock ramp. There is no strong reflected-ion beam in the foot region and weak current filaments are confined close to the shock front. This stage marks the beginning of a new shock-reformation cycle. By $t = 17.4\ \Omega_{\rm i}^{-1}$, a strong beam of reflected ions develops with $v_x \approx -v_{{\rm R},x}$ and flow-aligned plasma filaments appear in the shock foot (Figure 19(b)). As the beam traverses the foot region, the size of the filamentary precursor increases and reaches its maximum extension at $t \approx 18\ \Omega_{\rm i}^{-1}$ (Figure 19(c)). At the same time, a location of maximum ion reflection at the position of the mean cross-shock potential moves with the average plasma flow toward the shock ramp. On the shock ramp crossing, the shock potential structures become disrupted and converge with the downstream plasma flow. Current filaments start to merge ahead of the shock ramp which greatly enhances the bipolar electric fields associated with them. Once the gyration of ions in the shock foot forces the filaments to align closer with the shock surface, the electric field structures begin to play the role of new shock potential fields. Efficient ion reflection is thus set off in the region extending up to $\sim 3\ \lambda_{\rm si,R}$ from the shock ramp and continues until reflected-ion bunch becomes dispersed in the incoming plasma flow. By that time ($t \approx 18.6\ \Omega_{\rm i}^{-1}$, Figure 19 (d)), further filament mergers produce a new large-scale, quasi-coherent electric field potential structure at $\sim 2\ \lambda_{\rm si,R}$ from the shock ramp and a new shock-reformation cycle begins.

The simplified picture of shock self-reformation delineated above may be further modified by local effects resulting from a non-coherent evolution of current filaments across the shock. Phases of the reformation cycles thus change along the shock surface and partially cancel out in the average profiles of Figure 18, which makes the reformation irregular. Moreover, the shock-reformation process can also be influenced by the shock-front ripples. The latter was shown to modify the period of the reformation cycles in later stages in low-Mach-number perpendicular shocks (e.g., Hellinger et al. 2007; Lembège et al. 2009; Umeda et al. 2010). However, the rippling of the shock surface is weak in our case of a high-Mach-number forward shock and we do not see any apparent change of the reformation period throughout the duration of our simulation.

Finally, we note that cyclic self-reformation is also observed in the reverse shock. The physical nature of the process is the same as in the case of the forward shock. It is strongly influenced by shock rippling, and is visible only in the time evolution of the *local* electron density profiles (see, e.g., Umeda et al. 2010). Also in this case, the quasi-regular period of approximately 1.4 $\Omega_{\rm i}^{-1}$ does not change during the system evolution followed in our simulation.

4. SUMMARY AND DISCUSSION

We have performed 2D3V PIC simulations of non-relativistic plasma collisions with a perpendicular large-scale magnetic field. In the current study, we continue our investigation of the high-speed nonrelativistic shocks that started with the parallel shock simulations published in Niemiec et al. (2012). Here, the main question we addressed was how changing the magnetic field from a parallel to perpendicular configuration influences the resulting shock structure and the efficiency of particle pre-acceleration. By configuring the large-scale magnetic field at an angle of 45° to

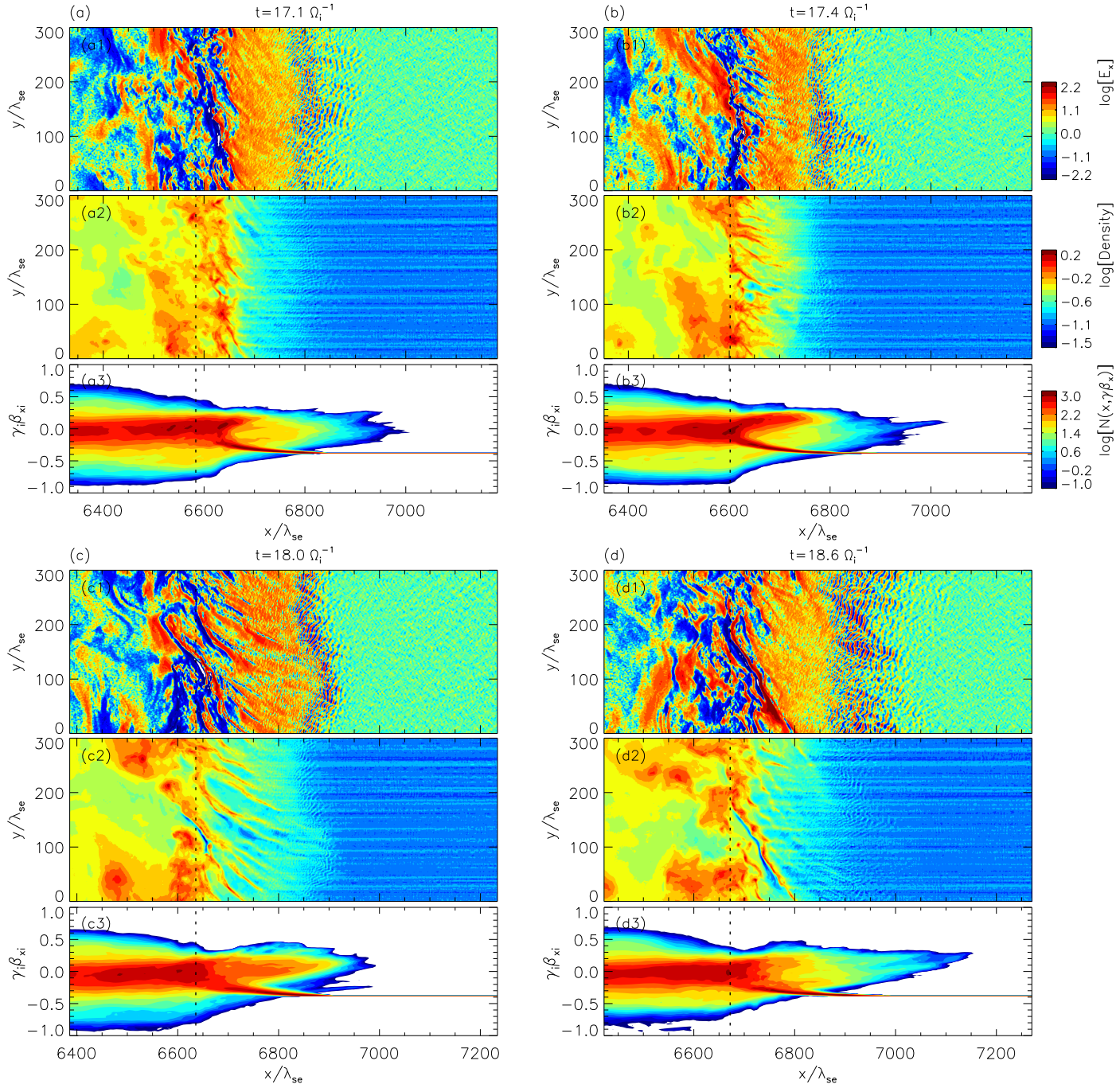

Figure 19. Structure of the forward shock in a series of snapshots at times (a) $t = 17.1\ \Omega_i^{-1}$, (b) $17.4\ \Omega_i^{-1}$, (c) $18\ \Omega_i^{-1}$, and (d) $18.6\ \Omega_i^{-1}$, illustrating the main phases of a shock self-reformation cycle. From top to bottom in each panel are displayed the distributions of the electric field component E_x, the density of electrons, and the longitudinal phase-space distribution of ions. The shock rest frame is used and the mean shock ramp position is marked with a dashed vertical line.

the simulation plane, we expect to approximate the 3D physics in a 2D system.

To address this question, we use a flow–flow setup with asymmetric plasma flows, i.e., utilizing the collision of plasma slabs of different density, leading to two different shocks and a CD that is self-consistently modeled. In contrast to the setup used by Murphy et al. (2010a, 2010b), we avoid the creation of an artificial dipole antenna at the CD by using a transition zone between full motional electric fields inside the plasmas and zero electric field in a small plasma-free area between the plasma flows at the beginning of the simulation. Therefore, with this new method, we ensure that our simulation is as clean as possible.

The simulation parameters are chosen such that they are close to those of a young SNR, and we use a reduced ion-to-electron mass ratio of $m_i/m_e = 50$ to capture both the electron and ion dynamics within the bounds of our simulation. The density ratio between the dense plasma and the tenuous plasma is 10, which is about the same ratio we would expect to find at a young SNR at the beginning of its free expansion phase in a typical ISM environment. However, the shock velocities we normally find in such an environment are about a factor of a

few lower than in our simulations. The sonic and Alfvénic Mach numbers of the forward shock are $M_{s,R} = 755$ and $M_{A,R} = 27.6$, respectively, and those of the reverse shock are $M_{s,L} = 252$ and $M_{A,L} = 28.5$, respectively. Here, as the forward and reverse shock, we denote the shocks propagating into the tenuous plasma and into the dense plasma, respectively.

Our results can be summarized as follows.

1. Our newly developed setup leads to the creation of a very clean perpendicular shock without artificial transients that may limit the veracity of the simulation. Eventually, a double-shock structure evolves within a few ion cyclotron times, Ω_i^{-1}. The shock transition is mediated by Weibel-type filamentation instabilities that lead to the development of current filaments and magnetic turbulence.
2. Shocks that form in the system are non-stationary and cyclically self-reform. As in low-Mach-number shocks, shock reformation is driven by a non-steady ion reflection. The period of reformation is similar at both shocks with $\sim 1.5\ \Omega_i^{-1}$. Generally, the periodicity of ion reflection is locally modified by the non-coherent evolution of current filaments across the shock.
3. The surface of the reverse shock is clearly rippled on the spatial and temporal scales given by the ions reflected at the shock. The ripples result from a modulation of the fraction of the shock-reflected ions along the shock surface, as in the scenario described by Burgess & Scholer (2007) for low-Mach-number shocks. Spatially modulated ion reflection at the shock should lead to enhanced localized electron heating and acceleration. The same instability operates in the forward shock, but its development is influenced by our boundary condition in the direction of the shock surface. We do not observe the inertia-scale fluctuations that would arise, e.g., from the AIC instability driven by temperature anisotropy at the shock ramp. The existence of ripples affects the visibility of shock reformation, which is washed out in the y-averaged density profiles of the reverse shock.
4. We do not find any evidence for gradient drift at the shock. It is not possible to reconstruct from the available electromagnetic field data a uniform drift direction because the local gradients in the turbulent magnetic field are much larger than the global gradient across the shock. We also do not find any indication of counterstreaming electrons and ions along the shock surface. In fact, the bulk motion of electrons and ions is commensurate with $\boldsymbol{E} \times \boldsymbol{B}$ drift in direction and amplitude. Note that the existence of an electric field component parallel to the drift direction of particles does not imply the existence of a significant electric field in the drift frame. In fact, in the guiding-center frame given by the local bulk motion and $\boldsymbol{E} \times \boldsymbol{B}$ drift, the electric field has a small amplitude, which explains the absence of electron acceleration in the ramp. For the ions, the guiding-center approximation is poorly justified, and so they may have trajectories along a significant electric field and be accelerated.
5. Downstream of both shocks, the electrons are well described by relativistic Maxwellians, suggesting that turbulence has been very efficient in relaxing the electron distribution function. Ion spectra are composed of a quasithermal bulk with $T_i/T_e \approx 2$ and a supra-thermal tail. We do not observe spectral variations with either distance from the shock or simulation time for $t \approx 5$–$20\ \Omega_i^{-1}$, suggesting a quasi-equilibrium in the system. The supra-thermal ions appear to result from SSA. The constancy of the maximum ion energy suggests that their spending more than a few gyro cycles in the shock region is exceptional. Electron heating arises from Buneman modes in the shock foot. Their amplitude is not high enough to prevent the escape of relativistic electrons, and so we observe heating of the bulk as opposed to the creation of a spectral tail. There is no evidence of the turbulent reconnection that was recently claimed to cause efficient electron energization (Matsumoto et al. 2015). The inefficient electron acceleration that we observed for low plasma beta and that Kato & Takabe (2010) observed for high plasma beta suggests that the plasma beta is not the deciding factor for the generation of a signicant non-thermal electron population. The ion-to-electron mass ratio in the simulation also does not play a role, since efficient acceleration has been observed in simulations with much lower $m_i/m_e = 25$, provided that suitable conditions for the nonlinear growth of the Buneman modes exist (Amano & Hoshino 2009b; Matsumoto et al. 2012). There may be additional factors in the microphysics of high-Mach-number shocks mediated by filamentation that limit the amplitude of Buneman waves or prevent the return of electrons to the foot region, resulting in a small number of supra-thermal electrons. To this end, the configuration of the large-scale magnetic field in 2D3V simulations may have an impact, as recent simulations showing significant tails in electron spectra have an orientation strictly out of plane (Matsumoto et al. 2012, 2013). Our setup with 45° orientation to the simulation plane should help to suppress such effects and allow 3D physics to be observed in 2D simulations. The lack of efficient electron acceleration in our simulation suggests a lower efficacy of kinetic instabilities in three dimensions with respect to specific 2D configurations. Fully three-dimensional studies of electron pre-acceleration at high-Mach-number shocks are clearly needed.

The authors thank Jens Ruppel for his contribution in preparing the new setup for the perpendicular shock. This work used the Extreme Science and Engineering Discovery Environment (XSEDE), which is supported by National Science Foundation grant number ACI-1053575. The authors acknowledge the Texas Advanced Computing Center (TACC) at The University of Texas at Austin for providing HPC and visualization resources that have contributed to the research results reported within this paper. We are also grateful for HPC resources provided by The North-German Supercomputing Alliance (HLRN). VW, MP, and IR acknowledge support through grants PO 1508/1-1 and PO 1508/1-2 of the Deutsche Forschungsgemeinschaft. The work of JN is supported by Narodowe Centrum Nauki through research projects DEC-2011/01/B/ST9/03183 and DEC-2013/10/E/ST9/00662. KN is supported by NSF AST-0908040, NNX12AH06G, NNX13AP-21G, and NNX13AP14G.

APPENDIX
DETAILS ON THE PERPENDICULAR SHOCK SETUP

To establish the transition zone, we taper off the magnetic field at the edge of both plasma slabs while keeping the plasma

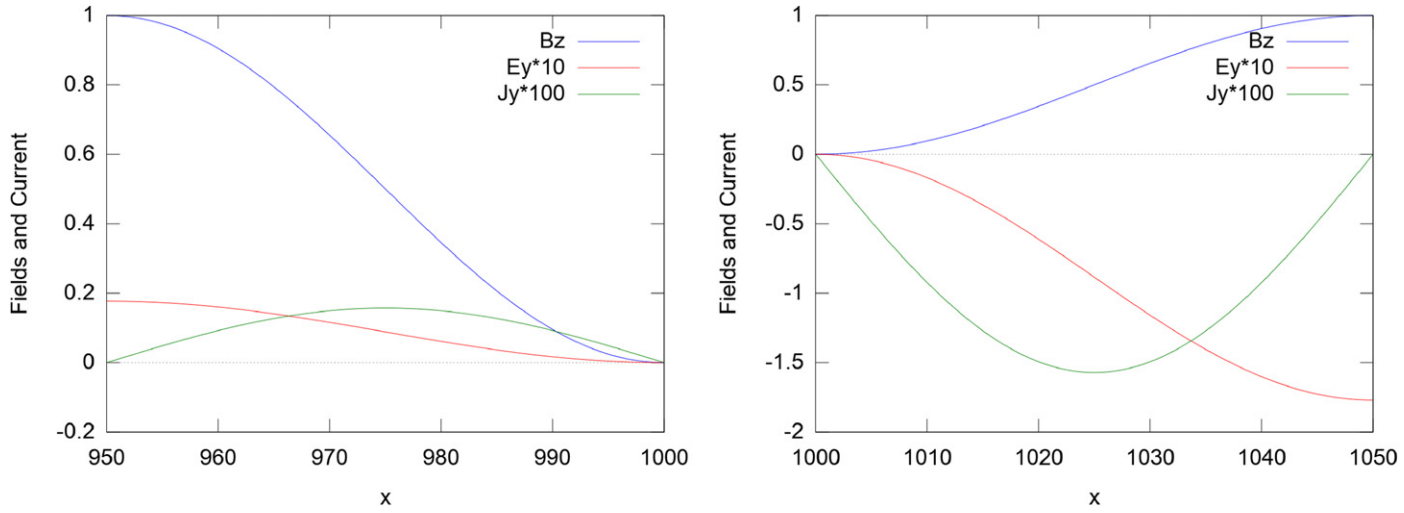

Figure 20. These two figures illustrate the setup of the transition zone in the left (left panel) and in the right (right panel) plasma for $\phi = 90°$. Shown are the perpendicular magnetic field B_z (blue), the motional electric field $E_y \times 10^1$ (red), and the current sheet $J_y \times 10^2$ (green). In this example, the width of the transition zone for both slabs is set to $w_{\rm grad} = 50\Delta$ and there is no plasma-free area between the beams.

density constant. The full homogeneous magnetic field of amplitude B_0 inside the left and right plasma spans a range from the left box boundary up to $x_{0\rm L}$ and from $x_{0\rm R}$ up to the right box boundary, respectively, while the transition zone extends from $x_{0\rm L}$ to $x_{0\rm L} + w_{\rm grad}$ and from $x_{0\rm R} - w_{\rm grad}$ to $x_{0\rm R}$, respectively. For the left transition zone, we set

$$\boldsymbol{B}_{\rm L}(x) = \frac{B_0}{2}\left[\cos\left(\frac{x - x_{0\rm L}}{w_{\rm grad}}\pi\right) + 1\right] \times (\cos(\phi)\hat{\boldsymbol{y}} + \sin(\phi)\hat{\boldsymbol{z}}), \quad (11)$$

where $\hat{\boldsymbol{y}}$ and $\hat{\boldsymbol{z}}$ are unit vectors in the y- and z-direction and we assume that the magnetic field vector $\boldsymbol{B}_0$ lies in the y–z plane at an angle ϕ to the y-axis. For the right transition zone, correspondingly we have

$$\boldsymbol{B}_{\rm R}(x) = \frac{B_0}{2}\left[\cos\left(\frac{x - x_{0\rm R}}{w_{\rm grad}}\pi\right) + 1\right] \times (\cos(\phi)\hat{\boldsymbol{y}} + \sin(\phi)\hat{\boldsymbol{z}}). \quad (12)$$

The factor of $1/2$ serves to normalize the term in brackets to values between 0 and 1. Outside the plasma slabs, the magnetic field is $B_y = B_z = 0$.

Note that whereas the magnetic field tapers off, the streaming velocity of the plasma slabs remains constant. The motional electric field in the transition zones thus follows the same profile as the magnetic field:

$$\boldsymbol{E}_{\rm L}(x) = \frac{v_{{\rm L},x}B_0}{2}\left[\cos\left(\frac{x - x_{0\rm L}}{w_{\rm grad}}\pi\right) + 1\right] \times (\sin(\phi)\hat{\boldsymbol{y}} - \cos(\phi)\hat{\boldsymbol{z}}), \quad (13)$$

and

$$\boldsymbol{E}_{\rm R}(x) = \frac{v_{{\rm R},x}B_0}{2}\left[\cos\left(\frac{x - x_{0\rm R}}{w_{\rm grad}}\pi\right) + 1\right] \times (\sin(\phi)\hat{\boldsymbol{y}} - \cos(\phi)\hat{\boldsymbol{z}}). \quad (14)$$

To achieve a stable gradient, one has to impose a current sheet in the transition zone that balances $\nabla \times \boldsymbol{B}$, so that in Heaviside–Lorentz units

$$\frac{\partial \boldsymbol{E}}{\partial t} = c\nabla \times \boldsymbol{B} - \boldsymbol{J} = 0. \quad (15)$$

As we have gradients only in the x-direction, the current density $\boldsymbol{J}$ has non-zero components in the y- and z-direction, namely, $J_y = -c\ \partial B_z/\partial x$ and $J_z = c\ \partial B_y/\partial x$. The current is set up through a drift of ions relative to the electrons, and as the particle density, n, is kept constant in the transition zone, $\boldsymbol{J} = n\ q\ \boldsymbol{v}_{\rm rel}$, the drift velocity $\boldsymbol{v}_{\rm rel}$ is calculated as

$$\boldsymbol{v}_{\rm rel,L}(x) = \frac{B_0\ c\pi}{2\ n_{\rm L}\ q\ w_{\rm grad}}\sin\left(\frac{x - x_{0\rm L}}{w_{\rm grad}}\pi\right) \times (\sin(\phi)\hat{\boldsymbol{y}} - \cos(\phi)\hat{\boldsymbol{z}}), \quad (16)$$

and

$$\boldsymbol{v}_{\rm rel,R}(x) = \frac{B_0\ c\pi}{2\ n_{\rm R}\ q\ w_{\rm grad}}\sin\left(\frac{x - x_{0\rm R}}{w_{\rm grad}}\pi\right) \times (\sin(\phi)\hat{\boldsymbol{y}} - \cos(\phi)\hat{\boldsymbol{z}}), \quad (17)$$

where $n_{\rm L}$ and $n_{\rm R}$ are the plasma particle densities in the left and the right plasma slabs, respectively.

The current is carried by ions to guarantee sufficient stability of the current sheet. For a suitable choice of $w_{\rm grad}$, the two plasmas fully collide after $2w_{\rm grad}/(v_{{\rm L},x} - v_{{\rm R},x}) \approx 1\ \Omega_{\rm e}^{-1} \approx 1/50\ \Omega_{\rm i}^{-1}$, implying that the current carried by the ions is directionally stable on the timescale of the plasma collision. We conducted tests to verify that no significant Buneman instabilities arise on account of the drift between electrons and ions. Therefore, all instabilities observed in our simulation arise solely from the collision. Figure 20 illustrates the setup of the transition zone for the out-of-plane perpendicular magnetic field orientation, i.e., $\phi = 90°$.

Figure 21 compares the stability in the particle density and field energy density of the standard setup with a constant perpendicular magnetic field B_z throughout the simulation box and the new setup with a transition zone as described above. One can clearly see that the new setup is very stable over many time steps, and the area between the plasmas stays largely free of electromagnetic fields until the plasma slabs smoothly

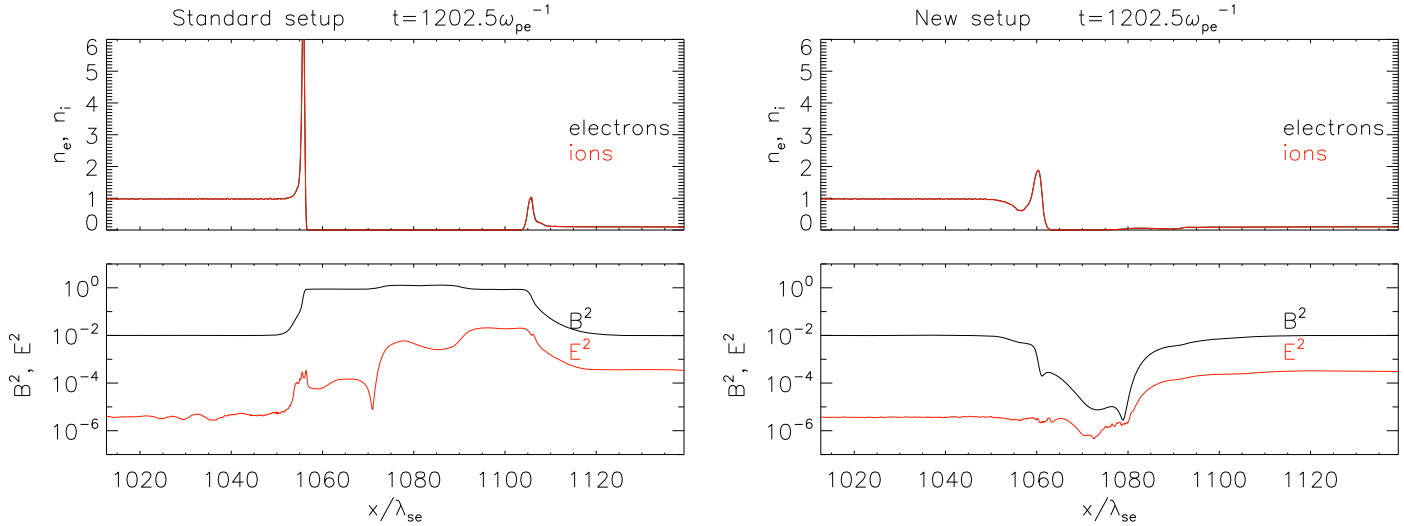

Figure 21. Stability comparison of the standard setup (constant perpendicular magnetic field B_z and jumping motional electric field E_y; left panel), and the new setup with the transition zone (right panel). Displayed is the state after 1202.5 ω_{pe}^{-1}, shortly before the collision of the two plasmas. Particle densities are shown in the top panels, whereas the lower panels display the field energy densities. In these demonstration simulations, the collision layer is at $x \approx 1063\ \lambda_{se}$ and the two plasma slabs started with $v_{L,x}$ and $v_{R,x}$, respectively, at $x = 1012.7\ \lambda_{se}$ and $x = 1519.0\ \lambda_{se}$.

collide with each other. In contrast, the standard method introduces strong transient fields and leads to strong density compressions at the fronts of the approaching plasma beams before the onset of the collision. One can observe a transient in the electric field which is emitted at the location of the sign flip in $\boldsymbol{E}$ in the middle of the simulation box, and which eventually perturbs the magnetic field. Note that in a realistic setup, the two plasma slabs are set much closer in the beginning than in this demonstration simulation; for example, for the setup with $w_{\rm grad} = 50\Delta$ shown in Figure 20, the plasmas fully collide after about 32 ω_{pe}^{-1}.

REFERENCES

Amano, T., & Hoshino, M. 2009a, PhPl, 16, 102901
Amano, T., & Hoshino, M. 2009b, ApJ, 690, 244
Baalrud, S. D., Callen, J. D., & Hegna, C. C. 2009, PhRvL, 102, 245005
Baalrud, S. D., Callen, J. D., & Hegna, C. C. 2010, PhPl, 17, 055704
Bale, S. D., Balikhin, M. A., Horbury, T. S., et al. 2005, SSRv, 118, 161
Ball, L., & Melrose, D. B. 2001, PASA, 18, 361
Blandford, R., & Eichler, D. 1987, PhR, 154, 1
Bret, A. 2015, JPlPh, 81, 455810202
Buneman, O. 1993, in Computer Space Plasma Physics, ed. H. Matsumoto, & Y. Omura (Tokyo: Terra Scientific)
Burgess, D., & Scholer, M. 2007, PhPl, 14, 012108
Burgess, D., Wilkinson, W. P., & Schwartz, S. J. 1989, JGRA, 94, 8783
Caprioli, D., & Spitkovsky, A. 2014, ApJ, 783, 91
Drake, J. F., Swisdak, M., Che, H., & Shay, M. A. 2006, Natur, 443, 553
Fermi, E. 1949, PhRv, 75, 1169
Friedman, A., Ambrosiano, J., Boyd, J., et al. 1990, in US-Japan Workshop on Advances in Simulation Techniques Applied to Plasmas and Fusion, LLNL Report UCRL-JC-106050
Ghavamian, P., Schwartz, S. J., Mitchell, J., Masters, A., & Laming, J. M. 2013, SSRv, 178, 633
Greenwood, A. D., Cartwright, K. L., Luginsland, J. W., & Baca, E. A. 2004, JCoPh, 201, 665
Guo, X., Sironi, L., & Narayan, R. 2014, ApJ, 794, 153
Hellinger, P., Trávníček, P., Lembège, B., & Savoini, P. 2007, GeoRL, 34, 14109
Ishihara, O., Hirose, A., & Langdon, A. B. 1980, PhRvL, 44, 1404
Kato, T. N., & Takabe, H. 2008, ApJL, 681, L93
Kato, T. N., & Takabe, H. 2010, ApJ, 721, 828
Krauss-Varban, D., Burgess, D., & Wu, C. S. 1989, JGR, 94, 15089
Krauss-Varban, D., & Wu, C. 1989, JGR, 94, 15367
Lampe, M., Haber, I., Orens, J. H., & Boris, J. P. 1974, PhFl, 17, 428
Lembege 2003, in Space Plasma Simulation, Vol. 615, ed. J. Büchner, C. Dum, & M. Scholer (Berlin: Springer)
Lembege, B., & Savoini, P. 1992, PhFlB, 4, 3533
Lembège, B., Savoini, P., Hellinger, P., & Trávníček, P. M. 2009, JGRA, 114, 3217
Leroy, M. M. 1983, PhFl, 26, 2742
Leroy, M. M., Goodrich, C. C., Winske, D., Wu, C.-C. S., & Papadopoulos, K. D. 1981, GeoRL, 8, 1269
Leroy, M. M., Winske, D., Goodrich, C. C., Wu, C. S., & Papadopoulos, K. D. 1982, JGRA, 87, 5081
Lowe, R. E., & Burgess, D. 2003, AnGeo, 21, 671
Matsukiyo, S., & Scholer, M. 2006, JGRA, 111, 6104
Matsumoto, Y., Amano, T., & Hoshino, M. 2012, ApJ, 755, 109
Matsumoto, Y., Amano, T., & Hoshino, M. 2013, PhRvL, 111, 215003
Matsumoto, Y., Amano, T., Kato, T. N., & Hoshino, M. 2015, Sci, 347, 974
Murphy, G. C., Dieckmann, M. E., Bret, A., & Drury, L. O. C. 2010a, A&A, 524, A84
Murphy, G. C., Dieckmann, M. E., & Drury, L. O. 2010b, PhPl, 17, 110701
Niemiec, J., Pohl, M., Bret, A., & Wieland, V. 2012, ApJ, 759, 73
Niemiec, J., Pohl, M., Stroman, T., & Nishikawa, K.-I. 2008, ApJ, 684, 1174
Omidi, N., & Winske, D. 1992, JGR, 97, 14801
Reynolds, S. P. 2008, ARA&A, 46, 89
Riquelme, M. A., & Spitkovsky, A. 2011, ApJ, 733, 63
Sagdeev, R., & Shapiro, V. 1973, JETPL, 17, 279
Shimada, N., & Hoshino, M. 2000, ApJL, 543, L67
Thomas, V. A. 1989, JGR, 94, 12009
Treumann, R. A. 2009, A&ARv, 17, 409
Treumann, R. A., & Jaroschek, C. H. 2008a, arXiv:0805.2181
Treumann, R. A., & Jaroschek, C. H. 2008b, arXiv:0806.4046
Umeda, T., Kidani, Y., Matsukiyo, S., & Yamazaki, R. 2014, PhPl, 21, 022102
Umeda, T., Kidani, Y., Yamao, M., Matsukiyo, S., & Yamazaki, R. 2010, JGRA, 115, 10250
Umeda, T., Yamao, M., & Yamazaki, R. 2008, ApJL, 681, L85
Umeda, T., Yamao, M., & Yamazaki, R. 2009, ApJ, 695, 574
Umeda, T., & Yamazaki, R. 2006, EP&S, 58, 41
Vay, J.-L. 2008, PhPl, 15, 056701
Winske, D., & Quest, K. B. 1988, JGR, 93, 9681